Historical and future development of the tidally averaged transport of sandy sediments in the Scheldt estuary

a 2D exploratory model

Boelens, Thomas; Schuttelaars, Henk; Plancke, Yves; De Mulder, Tom

Important note
To cite this publication, please use the final published version (if applicable).
Please check the document version above.

Historical and future development of the tidally averaged transport of sandy sediments in the Scheldt estuary: a 2D exploratory model

Thomas Boelens[1] (ID) · **Henk Schuttelaars[2]** · **Yves Plancke[3]** · **Tom De Mulder[1]**

Abstract

To investigate the historical development of the tidally averaged transport of sandy sediments in the main branch of the Scheldt estuary over the last decades (1950–2013), a 2D exploratory model has been developed. This model comprises the depth-averaged (2DH) shallow water equations, driven by an asymmetric tidal forcing at the seaward side, as well as an advection-diffusion equation to describe the depth-integrated dynamics of the suspended sediment concentration. The tidally averaged sand transport results from a subtle balance between the various contributions; advective contributions due to internally generated and externally prescribed overtides and the diffusive and topographically induced contributions. A seaward tidally averaged sand transport is found near the open boundary, whose magnitude has increased since ca. 1950. Moving upstream, the magnitude of the seaward transport decreases and changes into a smaller landward transport with a local maximum near the landward boundary. This maximum has increased over the years. Varying parameters that capture changes in the environment, e.g. historical changes in the bathymetry, future mean sea-level rise or changes in tidal forcing, results in changes in the tidally averaged sand transport that are systematically analysed and related to changes in the various contributions. Our model shows that there is a competition, in terms of determining the magnitude and the direction of the tidally averaged sand transport, between the effects of historical bathymetric changes, changes in tidal forcing and (projected) SLR. Even small changes in the tidal forcing at the seaward boundary can have a large impact on the magnitude and the direction of the tidally averaged sand transport. This hampers accurate predictions of sediment transport and morphodynamic changes in tidal systems, due to the uncertainty in the response of the tidal dynamics to the projected sea-level rise.

Keywords Sand transport · Scheldt estuary · 2DH exploratory model

1 Introduction

Estuaries and tidal rivers are highly dynamic systems, where the natural morphological development is the result of a complex interplay between water motion, sediment transport and bed topography. In most estuarine environments, tidesz are the most important forcing factor and the

✉ Thomas Boelens
thomas.boelens@ugent.be

1. Hydraulics Laboratory, Civil Engineering Department, Ghent University, Ghent, Belgium

2. Delft Institute of Applied Mathematics, Delft University of Technology, Delft, The Netherlands

3. Flanders Hydraulics Research, Antwerp, Belgium

morphological development is a result of the divergences in the residual or tidally averaged sediment transport. Therefore, mechanisms and processes influencing residual sediment transport play a key role in the development and understanding of how an estuary responds to changing natural forces and human interference (Chu et al. 2015).

In an estuary with a large tidal prism, the net sediment transport is the difference between two large numbers (import during flood and export during ebb). To accurately obtain this small difference from field measurements is very difficult, as sediment fluxes are hard to measure, requiring simultaneous flow and sediment concentration measurements across different cross-sections of the river (Bi and Toorman 2015). However, a good knowledge of the sediment transport is essential for planning of maintenance dredging activities and predicting the ecosystem services on the longer term (Temmerman et al. 2004; Kirwan et al. 2016).

The aim of this paper is to assess the influence of changing estuarine conditions, both historical and projected, on the residual transport of sandy materials and to gain a better understanding of the underlying physical transport mechanisms, by using a process-based numerical modelling approach. There are two different flavours of process-based modelling: simulation models on the one hand and exploratory or idealised models on the other (Murray 2003). In this paper, the exploratory model, developed in Boelens et al. (2018), will be extended and applied to the Scheldt Estuary.

Exploratory models aim at qualitatively reproducing the main trends and observations of the system by retaining only those processes that are believed to be important for the overall dynamics in an (often) schematised geometry. The key advantages of these models are their excellent ability to quickly investigate the sensitivity of the model outcomes to parameter variations and the possibility to systematically study physical processes in isolation (Murray 2003; Brouwer et al. 2018). However, only qualitative comparison with natural systems is possible, due to the idealised nature of these models and the interpretation of the results has to be conducted in the light of the underlying assumptions. Exploratory models have been used to study sediment dynamics in estuaries in e.g. Dronkers (1986) and Friedrichs et al. (1998) (analytical), Ridderinkhof et al. (2014) (1D), Chernetsky et al. (2010) and Dijkstra et al. (2017) (2DV), Boelens et al. (2018) (2DH) and Kumar et al. (2016), Wei et al. (2018), and Donatelli et al. (2018) (3D).

Simulation models try to reproduce a natural system as accurately as possible by implementing all known physical processes and state-of-the-art parameterisations. However, these models are in need of quantitative measurements for calibration and verification (Bi and Toorman 2015).

Furthermore, simulation models are computationally expensive, which hampers the performing of sensitivity studies. Moreover, simulation models have a limited suitability for long-term (decades to centuries) predictions (Wang et al. 2012) and the results can be difficult to interpret. Nevertheless, simulation models should be applied when a high level of accuracy is required. Simulation models have been used to study sediment dynamics in estuaries and salt marshes in e.g. Bolle et al. (2010), Fagherazzi et al. (2012), and van Maren et al. (2015).

To assess the (isolated) effects of changes in bathymetry, mean sea-level and tidal forcing on the residual transport of sandy sediments, we will focus on historical and projected changes in the Scheldt estuary (see Fig. 1). The Scheldt estuary has undergone several modifications since the mid-twentieth century. Since 1950, the area of the Western Scheldt has been reduced with about $141\,km^2$ (i.e. 8%) due to land reclamation at Sloe/Kaloot (next to Vlissingen), Braakman (next to Terneuzen) and Ossendrecht (van der Spek 1994; Vroon et al. 1997). Furthermore, there have been three periods of deepening and widening of the fairway ($1970 - 1975$, $1997 - 2001$, $2008 - 2010$), as well as a systematic maintenance dredging works (Meire and Van Dyck 2014). Since the 1950s, an annual amount of $2\,Mm^3$ of sand was extracted out the Western Scheldt for commercial purposes (Van der Werf and Briere 2013). Both natural evolution and the aforementioned human interferences (land reclamations, sand mining and fairway deepening) have considerably altered the bathymetry of the Scheldt estuary (Nnafie et al. 2018).

The mean sea level at the mouth of the estuary has increased with an average of 2.1 mm/year over the past century and with an average of 4.1 ± 1.5 mm/year between 1993 and 2011 (Wahl et al. 2013). Since mean high water

Fig. 1 The Scheldt estuary

has risen more than mean low water, the tidal range at the mouth of the estuary has increased as well. More upstream in the estuary, the tidal range has increased up to 10% in the last century (Barneveld et al. 2018).

Next to changes in bathymetry and mean sea level, also the tidal forcing at the mouth of the estuary has altered over the past century (Wang et al. 2002). This can have a large influence on the residual sediment transport, see Gräwe et al. (2014) and Müller et al. (2014).

Global mean sea level rise (SLR) will continue during the twenty-first century, very likely at a faster rate than observed from 1971 to 2010 (IPCC 2013). According to Pickering et al. (2012), there can be substantial changes in the tidal characteristics on the shelf seas, such as the North Sea. Large-scale models are used to predict the changes in the tidal dynamics under the influence of SLR, e.g. in Apecechea et al. (2017).

This paper is organised as follows. In Section 2, the adopted model and solution method will be outlined. This includes a detailed description and a schematisation of the Scheldt estuary and an extension of the model of Boelens et al. (2018) with a more accurate sediment concentration equation. Section 3 will present the model results, based on a historical and a recent situation in the Scheldt estuary. Subsequently, the sensitivity of the results to (future) changes in bathymetry, mean sea level and tidal forcing is discussed in Section 4. Finally, the main model results are summarised in Section 5.
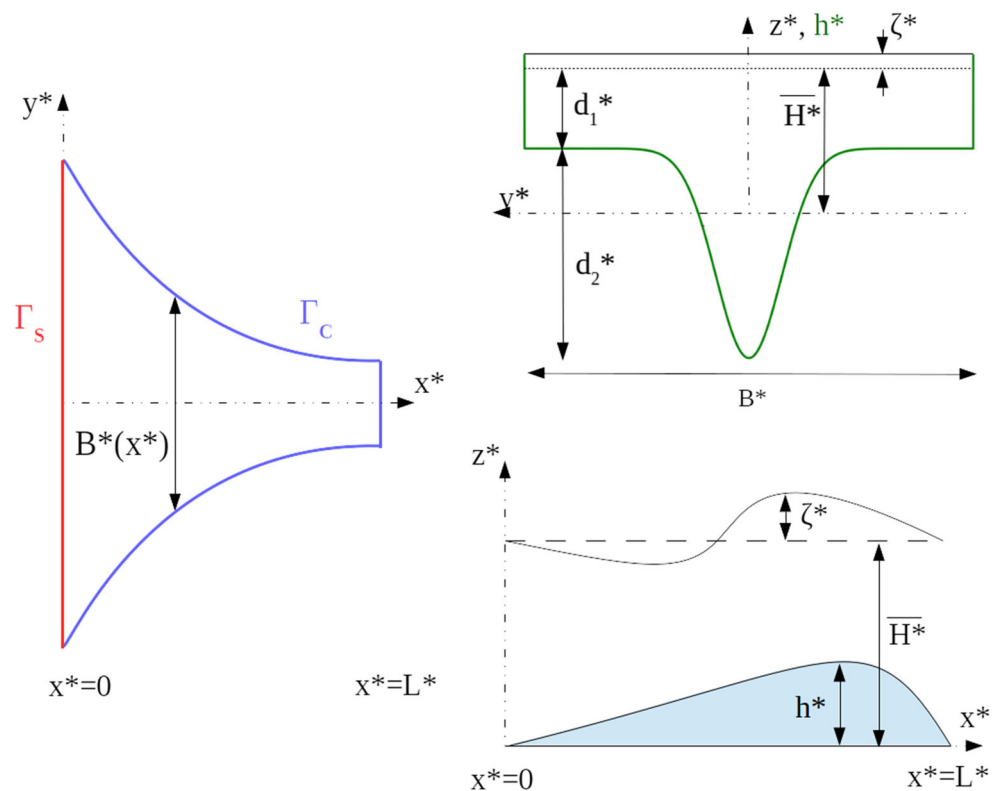
2 Model formulation

2.1 Geometry

The geometry considered is that of a semi-enclosed basin with length L^* (see Fig. 2), where the *-notation denotes a dimensional (unscaled) quantity. The schematised geometry of the basin and coordinate system is introduced in Fig. 2. The x^*-axis is oriented along the longitudinal axis of the basin, pointing in the landward direction, with the origin at the seaward side of the basin. The y^*-axis is oriented along the lateral axis, with the origin in the middle of the main channel. The total width, including the shallow zones, is denoted by $B^*(x^*)$ and varies along the channel. Based on data of yearly averaged values of the width at the water surface, the total width $B^*(x^*)$ will be defined as the average of the width at high and low water. This will be further eleborated in Section 3.1.

The local water depth is given by $\overline{H^*} - h^* + \zeta^*$, where $\overline{H^*}$ is the tidally and width-averaged water depth at the open boundary (the overbar notation denotes the average over the total width B^* at the open boundary). The sea surface elevation is denoted by ζ^* and is measured with respect to $z^* = \overline{H^*}$ (positively upwards). The bottom profile is denoted as $h^*(x^*, y^*)$. The shape of the bottom profile is taken from Li and O'Donnell (2005) and reads

$$h^*(x^*, y^*) = \overline{H^*} - d_1^*(x^*) - d_2^*(x^*)e^{-\left(y^*/\alpha_h^*(x^*)\right)^2}, \quad (1)$$

Fig. 2 Top view, cross-channel view and side view of a semi-enclosed tidal basin, flanked by shallow zones. For an explanation of the symbols, see the text

where a smaller α_h^* implies a narrower channel with steeper slopes. The bathymetry is symmetric with respect to the central axis of the estuary.

The boundary of the model domain consists of two parts. Solid boundaries are denoted by Γ_c and consist of vertical, non-erodible walls. Open boundaries are indicated by Γ_s and have a connection to the open sea.

2.2 Study area

The parameters introduced in the previous paragraph are derived from detailed bathymetric data of the Scheldt. The river Scheldt is 350 km long; it originates in France and flows through Belgium, towards the Netherlands, where it connects to the southern North Sea, through the Vlakte van de Raan. The part of the river, influenced by tides, extends 160 km from the mouth at Vlissingen to Ghent, where sluices impair the further propagation of the tidal wave (see Fig. 1). The estuary has a funnel-shaped geometry and its width reduces from about 6 km near the mouth to a couple of tens of meter near the head in Ghent. The width-averaged depth decreases non-linearly from 15 m at Vlissingen to only 3 m near Ghent (Wang et al. 2002). The saltwater influence typically reaches up to Temse (see Fig. 1) and the salinity can be regarded as vertically well mixed. The seaward (Dutch) part is referred to as the Western Scheldt while the Belgian part is called the Sea Scheldt and is mainly a single channel. Upstream of Dendermonde (see Fig. 1), the estuary is almost completely channelised (Hoffmann and Meire 1997). The Western Scheldt on the other hand has a complex and dynamic morphology. The flood and ebb channels are interconnected, bordered by large intertidal flats and salt marshes.

The tides in the Western Scheldt are dominantly semi-diurnal. The mean tidal prism is 2.2×10^9 m^3 at Vlissingen, 0.2×10^9 m^3 at the Belgian-Dutch border and 0.1×10^9 m^3 at Antwerp (Verlaan 1998). The mean tidal range increases between Vlissingen and about Temse from 3.8 to 5.5 m and decreases again to 1.9 m near Ghent (Hertoghs et al. 2018). The combined mean river outflow from the head and from the tributaries is about 120 m^3 s^{-1}, which accounts for a volume of 5×10^6 m^3 of water per semi-diurnal tide. This is less than 1% of the tidal prism at the down-estuarine

boundary. The maximum depth-averaged current velocities in the channels are in the order of $1 - 1.5$ m s^{-1} (Wang et al. 2002). Typical parameter values for a historical and a recent situation in the Scheldt estuary are given in Table 1.

2.3 Model equations

2.3.1 Hydrodynamics

Since the horizontal length scales are much larger than the typical water depth, the water motion can be described by the depth-averaged (2DH) shallow water equations, consisting of the continuity equation

$$\zeta_{t^*}^* + \nabla^* \cdot \left[(\overline{H^*} - h^* + \zeta^*)\mathbf{u}^* \right] = 0, \tag{2.2a}$$

and the momentum equation

$$\mathbf{u}_{t^*}^* + (\mathbf{u}^* \cdot \nabla^*)\mathbf{u}^* + g^* \nabla^* \zeta^* + f^* \mathbf{e}_{z^*} \times \mathbf{u}^* + \frac{r^* \mathbf{u}^*}{\overline{H^*} - h^* + \zeta^*} = 0, \tag{2.2b}$$

where $\mathbf{u}^* = (u^*, v^*)$ with u^* and v^* the depth-averaged velocity components in the x^* and y^* direction, respectively. Time is denoted as t^* and g^* is the acceleration due to gravity. The Coriolis coefficient is $f^* = 2\Omega^* \sin\varphi$, with Ω^* the rotation rate of the earth and φ the latitude. The unit vector in the z-direction is denoted by $\mathbf{e}_{z^*}$ and $\nabla^* = (\partial/\partial x^*, \partial/\partial y^*)$ is the horizontal gradient. The Reynolds stresses, related to turbulent exchange of momentum in the horizontal direction, are neglected and no density gradients or wind effects are taken into account. The last contribution on the left-hand side of Eq. 2.2b is the bed shear stress, divided by the product of the water density ρ^* and the local water depth. Here, a linearised formulation of the bed shear stress, the so-called Lorentz linearisation (Lorentz 1922; Zimmerman 1982), is adopted, where r^* is a friction coefficient with physical units m s^{-1}, that is assumed constant across the entire domain.

The water motion is forced at the seaward entrance of the estuary by a prescribed sea surface elevation, consisting of M_2 and M_4 tidal constituents. At the landward side and at the sidewalls, the water transport is required to vanish. Note that this implies that river flow is not accounted for. The boundary conditions can then be written as

$$\zeta^* = A_{M_2}^* \cos(\sigma^* t^* - \theta_{M_2}) + A_{M_4}^* \cos(2\sigma^* t^* - \theta_{M_4}) \quad \text{for } (x^*, y^*) \in \Gamma_s, \tag{2.3a}$$

$$\mathbf{u}^* \cdot \mathbf{n} = 0 \qquad \qquad \text{for } (x^*, y^*) \in \Gamma_c, \tag{2.3b}$$

with $A_{M_2}^*$ the amplitude, θ_{M_2} the phase and σ^* the angular frequency of the semidiurnal tidal component of the water level. The quantity $A_{M_4}^*$ is the amplitude and θ_{M_4} the phase of the quarter diurnal constituent of the water level. It should

be noted that $A_{M_2}^*$, θ_{M_2}, $A_{M_4}^*$ and θ_{M_4} all depend on the x^* and y^* coordinates of the points along the seaward boundary Γ_s. Finally, $\mathbf{n}$ is the outward pointing normal unit vector at the solid boundary Γ_c.

Table 1 Dimensional values for the model parameters, based on a historical and a recent situation in the Scheldt estuary

General parameters			
Length	$L^* = 160\,\text{km}$	Gravitational accelaration	$g^* = 9.81\,\text{ms}^{-2}$
Tidally averaged water depth	$\overline{H^*} = 14.73\,\text{m}\ (13.71\,\text{m})$	Coriolis frequency	$f^* = 1.13 \times 10^{-4}\,\text{s}^{-1}$
Tidal parameters			
M_2 water level amplitude	$\overline{A^*_{M_2}} = 1.77\,\text{m}\ (1.68\,\text{m})$	M_2 water level phase	$\overline{\theta_{M_2}} = 0°$
M_4 water level amplitude	$\overline{A^*_{M_4}} = 0.14\,\text{m}\ (0.11\,\text{m})$	M_4 water level phase	$\overline{\theta_{M_4}} = -1.3°\ (-5.4°)$
Angular frequency	$\sigma^* = 1.4 \times 10^{-4}\,\text{s}^{-1}$	Friction parameter	$r^* = 1.7 \times 10^{-3}\,\text{m s}^{-1}$
Sediment parameters			
Horizontal diffusivity	$\mu^* = 100\,\text{m}^2\,\text{s}^{-1}$	Vertical diffusion coefficient	$\kappa^*_v = 0.1\,\text{m}^2\,\text{s}^{-1}$
Settling velocity	$w^*_s = 0.02\,\text{m s}^{-1}$	Erosion parameter	$\alpha^* = 0.01\,\text{kg s m}^{-4}$
Dimensionless	**Order**		
$\epsilon = \frac{\overline{A^*_{M_2}}}{\overline{H^*}} = 0.12\ (0.12)$	$\mathcal{O}(\epsilon)$	$\overline{\gamma} = \frac{\overline{A^*_{M_4}}}{\overline{A^*_{M_2}}} = 0.08\ (0.07)$	$\mathcal{O}(\epsilon)$
$\eta = \frac{\sigma * L^*}{\sqrt{g^* \overline{H^*}}} = 1.86\ (1.93)$	$\mathcal{O}(1)$	$r = \frac{r^*}{\sigma * \overline{H^*}} = 0.82\ (0.89)$	$\mathcal{O}(1)$
$f = \frac{f^*}{\sigma *} = 0.81$	$\mathcal{O}(1)$	$a = \frac{\sigma^* \kappa^*_v}{(w^*_s)^2} = 0.035$	$\mathcal{O}(\epsilon^2)$
$\mu = \frac{\mu^*}{\sigma *(L^*)^2} = 2.8 \times 10^{-5}$	$\mathcal{O}(\epsilon^5)$	$\Lambda = \frac{w^*_s \overline{H^*}}{\kappa^*_v} = 2.95\ (2.74)$	$\mathcal{O}(1)$

The values for the historical situation are given between brackets, in case they differ from the recent situation. For further information we refer to the main text

2.3.2 Sand transport

To evaluate how the basin geometry and the tidal forcing affect the net transport of sandy material (here consisting of non-cohesive material with a single grain size of $\sim 2 \times 10^{-4}$ m), a simple sediment transport formula is used. The fine sandy material is assumed to be transported predominantly as suspension load. Following Ter Brake and Schuttelaars (2010) and the supplementary material of de Swart and Zimmerman (2009) and Burchard et al. (2018), the temporal evolution of the suspended sediment concentration can be modelled using a depth-integrated advection-diffusion equation:

$$C^*_{t^*} + \nabla^* \cdot \underbrace{\left(\mathbf{u}^* C^* - \mu^* \nabla^* C^* - \mu^* \frac{w^*_s}{\kappa^*_v} \beta C^* \nabla^* h^* \right)}_{\mathbf{q}^*}$$
$$= \alpha^* |\mathbf{u}^*|^2 - \frac{(w^*_s)^2}{\kappa^*_v} \beta C^*, \tag{2.4}$$

where C^* is the depth-integrated sediment concentration, μ^* the horizontal diffusion coefficient, κ^*_v the vertical diffusion coefficient, w^*_s the settling velocity and α^* a constant erosion parameter. Typical values of these parameters can be found in Table 1. Furthermore, $\mathbf{q}^* =$

(q^*_u, q^*_v) denotes the depth-integrated, tidally averaged suspended sediment transport. Finally, the dimensionless, depth-dependent deposition parameter β is defined as

$$\beta = \left[1 - e^{-\frac{w^*_s}{\kappa^*_v}(\overline{H^*} - h^* + \zeta^*)} \right]^{-1}. \tag{2.4}$$

The depth-integrated sediment concentration C^* with dimension (kg m^{-2}) refers to the total amount of sediment stored in a water column with unit horizontal area. The first contribution on the right-hand side of Eq. 2.4 models the whirling up of sediment from the bed, due to shear stresses exerted on the bed. As we only consider transport of fine sand in this paper, the critical velocity of motion is small compared with the tidal velocity during the largest part of a tidal cycle. Therefore, as a first approximation, we set the critical velocity for erosion to zero. The second contribution on the right-hand side of Eq. 2.4 models the deposition of sediment. The first contribution on the left-hand side of Eq. 2.4 is the local inertia of the concentration. The second term is the divergence of the advective sediment transport, while the third and fourth terms model the diffusive contributions. More precisely, the fourth term on the left-hand side represents the convergence and divergence of the horizontal diffusive sediment flux induced by topographic variations. The occurrence of this sediment flux can be

easily understood if one considers the vertical distribution of sediment in the water. The concentration is highest near the bed and reduces with decreasing depth. Therefore, at a fixed depth, the sediment concentration is higher in the shallower areas than in the deeper areas. Hence, there is a horizontal concentration gradient between these regions, resulting in a diffusive sediment transport directed towards the deeper water area (for more information and a derivation, see Ter Brake and Schuttelaars (2010)).

At the landward side and at the sidewalls, the suspended load transport is required to vanish. At the seaward entrance, a balance between erosion and deposition is imposed as a boundary condition for the tidally averaged sediment concentration. Concerning the time-dependent components of the concentration, we require that no diffusive boundary layer develops at the seaward side (see Schuttelaars and de Swart (2000)). This leads to the following boundary conditions

$$\left\langle \alpha^* |\mathbf{u}^*|^2 - \frac{(w_s^*)^2}{\kappa_v^*} \beta C^* \right\rangle = 0 \qquad \text{for } (x^*, y^*) \in \Gamma_s, \tag{2.6a}$$

$$\tilde{C}^*(x^*, y^*, t^*, \mu^*) = \tilde{C}^*(x^*, y^*, t^*, \mu^* = 0) \qquad \text{for } (x^*, y^*) \in \Gamma_s, \tag{2.6b}$$

$$\left(\mathbf{u}^* C^* - \mu^* \nabla^* C^* - \mu^* \frac{w_s^*}{\kappa_v^*} \beta C^* \nabla^* h^* \right) \cdot \mathbf{n} = 0 \qquad \text{for } (x^*, y^*) \in \Gamma_c, \tag{2.6c}$$

where $\langle . \rangle$ denotes the tidal average, defined as $\frac{1}{T} \int_T \cdot \, dt$, with T the tidal period, and $\tilde{C}^* = C^* - \langle C^* \rangle$. Note, that the boundary conditions for the sediment concentration Eq. 2.6c and velocities Eq. 2.3b imply that no sand transport $\mathbf{q}^*$ takes place through the closed boundaries Γ_c. The tidally and depth-averaged suspended sediment concentration (SSC) [kg/m³] can then be estimated as

$$\text{SSC} = \left\langle \frac{C^*}{\overline{H^*} - h^* + \zeta^*} \right\rangle. \tag{2.7}$$

In this contribution, we do not consider the feedback of the divergence and convergence of the sand transport on the bed evolution, i.e. we focus on the initial transport only: for a given bathymetry, this approach gives insight in how the bottom tends to adapt initially. For changes on the long term, adaptations to the model are required, such that the morphodynamics is taken into account explicitly, e.g. by calculation of equilibrium bathymetries (Schuttelaars and de Swart 2000; Ter Brake and Schuttelaars 2011).

2.4 Dimensionless equations

The governing equations are made dimensionless by introducing characteristic scales for the physical variables (dimensionless variables are denoted without an asterisk):

$$(x^*, y^*) = L^*(x, y); \quad (u^*, v^*) = U^*(u, v); \quad \zeta^* = \overline{A_{M_2}^*} \zeta;$$

$$(z^*, h^*) = \overline{H^*}(z, h); \quad t^* = \sigma^{*-1} t; \quad r^* = (\sigma^* \overline{H^*}) r;$$

$$f^* = \sigma^* f; \quad \mu^* = \sigma^* (L^*)^2 \mu; \quad C^* = \frac{\alpha^* (U^*)^2 \kappa_v^*}{(w_s^*)^2} C. \tag{2.8}$$

The characteristic scales include the length L^* of the basin, the tidally and width-averaged water depth at the open boundary $\overline{H^*}$, the width-averaged water level amplitude at the open boundary $\overline{A_{M_2}^*}$ and angular frequency σ of the semidiurnal tide. The velocity scale follows from the continuity Eq. 2.2a and reads $U^* = \sigma^* \overline{A_{M_2}^*} L^* / \overline{H^*}$, while the friction scale and Coriolis scale follow from the momentum equation. Finally, the sediment concentration equation determines the scaling for the horizontal diffusion coefficient and for the depth-integrated suspended sediment concentration. The latter is scaled with the ratio of the coefficients of the erosion term $\alpha(U^*)^2$ and the deposition term $(w_s^*)^2 / \kappa_v^*$, which implies that erosion and deposition are approximately balancing each other. The dimensionless equations for the water motion read

$$\zeta_t + \nabla \cdot [(1 - h + \epsilon \zeta) \mathbf{u}] = 0, \tag{2.9a}$$

$$(1 - h + \epsilon \zeta) \left[u_t + \epsilon (\mathbf{u} \cdot \nabla) \mathbf{u} + \eta^{-2} \nabla \zeta + f \mathbf{e}_z \times \mathbf{u} \right] + r\mathbf{u} = 0, \tag{2.9b}$$

where the momentum equation has been multiplied with the local water depth (i.e. $1 - h + \epsilon \zeta$). The parameter $\eta = (\sigma^* L^*) / \sqrt{g^* \overline{H^*}}$ in Eq. 2.9b is, apart from a factor 2π, the ratio of the estuary length, L^*, and the frictionless tidal wavelength in a straight channel without tidal flats $L_g^* = 2\pi \sqrt{g^* \overline{H^*}} / \sigma^*$. Furthermore, the parameter $\epsilon =$

$\overline{A^*_{M_2}}/\overline{H^*} = U^*/(\sigma^* L^*)$ is the ratio of the semidiurnal water level amplitude and the tidally and width-averaged water depth at the open boundary, as well as the ratio of the tidal excursion (the distance travelled by a fluid particle in a tidal period) and the estuary length. The parameter ϵ is usually small.

The dimensionless concentration equation becomes

$$a\left[C_t + \nabla \cdot (\epsilon \mathbf{u} C - \mu \nabla C - \mu \Lambda \beta C \nabla h)\right] = |\mathbf{u}|^2 - \beta C. \tag{2.10}$$

Here $a = \frac{\sigma^* \kappa^*_v}{(w^*_s)^2}$ is the ratio of the deposition time scale over the tidal time scale and $\Lambda = \frac{w^*_s \overline{H^*}}{\kappa^*_v}$ is the sediment Peclet number, which is the ratio of the typical time it takes a particle to settle in the water column and the typical time needed to mix particles through the water column. The dimensionless deposition parameter β can be written in terms of dimensionless variables as

$$\beta = \left[1 - e^{-\Lambda(1-h+\epsilon\zeta)}\right]^{-1}. \tag{2.11}$$

The dimensionless boundary conditions read

$$\zeta = A_{M_2}\cos(t - \theta_{M_2}) + \gamma\cos(2t - \theta_{M_4}) \quad \text{for } (x, y) \in \Gamma_s, \tag{2.12a}$$

$$\left\langle |\mathbf{u}|^2 - \beta C \right\rangle = 0 \quad \text{for } (x, y) \in \Gamma_s, \tag{2.12b}$$

$$\tilde{C}(x, y, t, \mu) = \tilde{C}(x, y, t, \mu = 0) \quad \text{for } (x, y) \in \Gamma_s, \tag{2.12c}$$

$$\mathbf{u} \cdot \mathbf{n} = 0 \quad \text{for } (x, y) \in \Gamma_c, \tag{2.12d}$$

$$(\epsilon \mathbf{u} C - \mu \nabla C - \mu \Lambda \beta C \nabla h) \cdot \mathbf{n} = 0 \quad \text{for } (x, y) \in \Gamma_c, \tag{2.12e}$$

where $A_{M_2} = A^*_{M_2}/\overline{A^*_{M_2}}$ and $\gamma = A^*_{M_4}/\overline{A^*_{M_2}}$. Note that $A_{M_2}, \theta_{M_2}, \gamma$ and θ_{M_4} depend on the x and y coordinates at the seaward boundary Γ_s.

2.5 Solution method

The result of the scaling procedure, described above, is that the magnitudes of all terms in the governing equations are measured by dimensionless numbers. Reference values can be found in Table 1. Relating these dimensionless numbers to ϵ, the relative importance of each term can be assessed.

2.5.1 Perturbation approach

This allows for solving (2.9a), together with boundary conditions Eq. 2.12a, by making an expansion of the physical variable χ in the small parameters ϵ and $\overline{\gamma}$, where χ is any of the hydrodynamic variables ζ, u or v. Here, $\overline{\gamma}$ is the ratio of the width-averaged M_4 and M_2 amplitudes of the water level at the open boundary. According to Table 1, ϵ and $\overline{\gamma}$ are of the same order of magnitude, but we consider them separately. This allows for making

a distinction between internally generated and externally prescribed overtides. Up to first order, the asymptotic expansion reads

$$\chi = \chi^{00} + \epsilon\chi^{10} + \overline{\gamma}\chi^{01} + \dots \tag{2.13}$$

The first superscript gives the order in ϵ and the second one the order in $\overline{\gamma}$. Inserting these expressions in the equations and collecting terms of similar order in ϵ and $\overline{\gamma}$ result in systems of equations at different order.

Similarly, the sediment concentration equation can be solved using an asymptotic approach, with

$$C = C^{00} + \epsilon C^{10} + \overline{\gamma}C^{01} + \dots \tag{2.14}$$

To this end, the deposition parameter β (which does not contain $\overline{\gamma}$) has to be expanded in the small parameter ϵ only. The leading and first order contributions read

$$\beta^{00} = \frac{1}{1 - e^{-\Lambda(1-h)}}, \qquad \beta^{10} = -\frac{\Lambda\zeta^{00}e^{-\Lambda(1-h)}}{\left(1 - e^{-\Lambda(1-h)}\right)^2}. \tag{2.15}$$

Collecting terms independent of the small parameters ϵ and $\overline{\gamma}$ results in the leading order system of equations:

$$\boxed{\mathcal{O}(1)} \qquad \zeta^{00}_t + \nabla \cdot \left[(1-h)\mathbf{u}^{00}\right] = 0, \tag{2.16a}$$

$$(1-h)\left(\mathbf{u}^{00}_t + \eta^{-2}\nabla\zeta^{00} + f\mathbf{e}_z \times \mathbf{u}^{00}\right) + r\mathbf{u}^{00} = 0, \tag{2.16b}$$

$$a\left[C^{00}_t + \nabla \cdot \left(-\mu\nabla C^{00} - \mu\Lambda\beta^{00}C^{00}\nabla h\right)\right] = |\mathbf{u}^{00}|^2 - \beta^{00}C^{00}, \tag{2.16c}$$

with boundary conditions

$$\zeta^{00} = A_{M_2} \cos(t - \theta_{M_2}) \qquad \text{for } (x, y) \in \Gamma_s, \tag{2.17a}$$

$$\mathbf{u}^{00} \cdot \mathbf{n} = 0 \qquad \text{for } (x, y) \in \Gamma_c, \tag{2.17b}$$

$$\left\langle |\mathbf{u}^{00}|^2 - \beta^{00} C^{00} \right\rangle = 0 \qquad \text{for } (x, y) \in \Gamma_s, \tag{2.17c}$$

$$\tilde{C}^{00}(x, y, t, \mu) = \tilde{C}^{00}(x, y, t, \mu = 0) \qquad \text{for } (x, y) \in \Gamma_s, \tag{2.17d}$$

$$\left(-\mu \nabla C^{00} - \mu \Lambda \beta^{00} C^{00} \nabla h \right) \cdot \mathbf{n} = 0 \qquad \text{for } (x, y) \in \Gamma_c, \tag{2.17e}$$

with A_{M_2} and θ_{M_2} depending on the x and y coordinates along Γ_s.

At order ϵ, the water motion and sediment concentration are described by

$$\boxed{\mathcal{O}(\epsilon)} \qquad \zeta_t^{10} + \nabla \cdot \left[(1 - h)\mathbf{u}^{10} \right] + \nabla \cdot \left(\zeta^{00} \mathbf{u}^{00} \right) = 0, \tag{2.18a}$$

$$(1 - h) \left[\mathbf{u}_t^{10} + \eta^{-2} \nabla \zeta^{10} + f \mathbf{e}_z \times \mathbf{u}^{10} + \left(\mathbf{u}^{00} \cdot \nabla \right) \mathbf{u}^{00} \right]$$
$$+ \zeta^{00} \left[\mathbf{u}_t^{00} + \eta^{-2} \nabla \zeta^{00} + f \mathbf{e}_z \times \mathbf{u}^{00} \right] + r \mathbf{u}^{10} = 0, \tag{2.18b}$$

$$a \left\{ C_t^{10} + \nabla \cdot \left[\mathbf{u}^{00} C^{00} - \mu \nabla C^{10} - \mu \Lambda \left(\beta^{10} C^{00} \nabla h + \beta^{00} C^{10} \nabla h \right) \right] \right\}$$
$$= 2\mathbf{u}^{00} \cdot \mathbf{u}^{10} - \beta^{00} C^{10} - \beta^{10} C^{00}, \tag{2.18c}$$

with boundary conditions

$$\zeta^{10} = 0 \qquad \qquad \text{for } (x, y) \in \Gamma_s, \tag{2.19a}$$

$$\mathbf{u}^{10} \cdot \mathbf{n} = 0 \qquad \qquad \text{for } (x, y) \in \Gamma_c. \tag{2.19b}$$

$$\tilde{C}^{10}(x, y, t, \mu) = \tilde{C}^{10}(x, y, t, \mu = 0) \qquad \qquad \text{for } (x, y) \in \Gamma_s, \tag{2.19c}$$

$$\left[\epsilon \mathbf{u}^{00} C^{00} - \mu \nabla C^{10} - \mu \Lambda (\beta^{10} C^{00} \nabla h + \beta^{00} C^{10} \nabla h) \right] \cdot \mathbf{n} = 0 \qquad \text{for } (x, y) \in \Gamma_c. \tag{2.19d}$$

At order $\overline{\gamma}$, the system of equations reduces to

$$\boxed{\mathcal{O}(\overline{\gamma})} \qquad \zeta_t^{01} + \nabla \cdot \left[(1 - h)\mathbf{u}^{01} \right] = 0, \tag{2.20a}$$

$$(1 - h) \left(\mathbf{u}_t^{01} + \eta^{-2} \nabla \zeta^{01} + f \mathbf{e}_z \times \mathbf{u}^{01} \right) + r \mathbf{u}^{01} = 0, \tag{2.20b}$$

$$a \left[C_t^{01} + \nabla \cdot \left(-\mu \nabla C^{01} - \mu \Lambda \beta^{00} \nabla h C^{01} \right) \right] = 2\mathbf{u}^{00} \cdot \mathbf{u}^{01} - \beta^{00} C^{01}, \tag{2.20c}$$

with boundary conditions

$$\zeta^{01} = \frac{\gamma}{\overline{\gamma}} \cos(2t - \theta_{M_4}) \qquad \text{for } (x, y) \in \Gamma_s, \tag{2.21a}$$

$$\mathbf{u}^{01} \cdot \mathbf{n} = 0 \qquad \text{for } (x, y) \in \Gamma_c \tag{2.21b}$$

$$\tilde{C}^{01}(x, y, t, \mu) = \tilde{C}^{01}(x, y, t, \mu = 0) \qquad \text{for } (x, y) \in \Gamma_s, \tag{2.21c}$$

$$\left(-\mu \nabla C^{01} - \mu \Lambda \beta^{00} \nabla h C^{01} \right) \cdot \mathbf{n} = 0 \qquad \text{for } (x, y) \in \Gamma_c, \tag{2.21d}$$

and γ and θ_{M_4} depending on the x and y coordinates along the open boundary Γ_s. This approach clearly shows that the overtides consist of an externally prescribed (χ^{01}) and an internally generated part (χ^{10}). The externally prescribed part is only driven by the sea surface elevation at the open boundary Eq. 2.21a and is independent of the semidiurnal components. The internally generated part originates from the non-linear interactions of the semidiurnal components, i.e. the non-linear terms in Eq. 2.18a.

Inspecting the leading order system and its forcings, it can be deduced that at leading order, the water motion only consists of semidiurnal tidal components. At first order in ϵ, the non-linearities generate tidally averaged components and overtides with a double frequency, while at first order in $\overline{\gamma}$ only overtides with a double frequency are present. Hence, the hydrodynamic variables can be written as

$$\chi^{00}(x, y, t) = \chi_{s1}^{00}(x, y) \sin t$$
$$+ \chi_{c1}^{00}(x, y) \cos t, \quad (2.22a)$$
$$\chi^{10}(x, y, t) = \left\langle \chi^{10}(x, y) \right\rangle + \chi_{s2}^{10}(x, y) \sin(2t)$$
$$+ \chi_{c2}^{10}(x, y) \cos(2t), \quad (2.22b)$$
$$\chi^{01}(x, y, t) = \chi_{s2}^{01}(x, y) \sin(2t)$$
$$+ \chi_{c2}^{01}(x, y) \cos(2t). \quad (2.22c)$$

where χ_{s1}^{00} and χ_{c1}^{00} denote the spatially varying amplitudes of the sine and cosine components of the main tidal component (M_2), respectively. The tidally averaged contributions generated by non-linear interactions are denoted by $\left\langle \chi^{10} \right\rangle$, whereas χ_{s2}^{10} and χ_{c2}^{10} are the amplitudes of the sine and cosine components of the internally generated M_4 overtide. The coefficients χ_{s2}^{01} and χ_{c2}^{01} are the amplitudes of the sine and cosine components of the externally prescribed M_4 overtide, respectively. Equation 2.22a can be rewritten in terms of phases and amplitudes as

$$\chi = \chi_{M_2}^{amp} \cos(t - \chi_{M_2}^{pha})$$
$$+ \epsilon \left(\chi_{M_0}^{amp} + \chi_{M_4}^{amp,int} \cos(2t - \chi_{M_4}^{pha,int}) \right)$$
$$+ \overline{\gamma} \chi_{M_4}^{amp,ext} \cos(2t - \chi_{M_4}^{pha,ext}) + \text{h.o.t.}, \quad (2.13)$$

with $\chi_{M_2}^{amp} = \sqrt{(\chi_{c1}^{00})^2 + (\chi_{s1}^{00})^2}$, the amplitude and $\chi_{M_2}^{pha} = \arctan(\chi_{s1}^{00}/\chi_{c1}^{00})$ the phase of the semidiurnal tidal constituent (which has to be taken in the correct quadrant) and

$\chi_{M_0}^{amp} = \left\langle \chi^{10} \right\rangle$ is the amplitude of the tidally averaged contribution. The amplitude and phase of the overtide, which consists of an externally prescribed ($\chi_{M_4}^{amp,ext}, \chi_{M_4}^{pha,ext}$) and an internally generated ($\chi_{M_4}^{amp,int}, \chi_{M_4}^{pha,int}$) part, are defined analogously. The total M_4 amplitude or phase is not equal to the sums of the externally prescribed and internally generated parts, since these two parts interfere with each other.

Regarding the sediment concentration, the leading order concentration terms are forced by non-linear interactions of the leading order M_2 velocity through the erosion term (see Eq. 2.16c). Using Eq. 2.13, it follows that in leading order, the sediment concentration consists of a tidally averaged component and a component with a double frequency. Furthermore, the order-ϵ concentrations are generated by the interaction of the M_2 water motion and the internally generated overtides through the erosion term and through the advection of the leading order suspended sediment concentration by the leading order tidal velocity. Finally, the order-$\overline{\gamma}$ concentrations are generated by the interaction of the M_2 tidal signal and the externally prescribed M_4 tidal forcing through the erosion term. Careful inspection of equations Eqs. 2.18c and 2.20c, together with equaton Eq. 2.13, shows that at first order in ϵ and $\overline{\gamma}$, the sediment concentration consists of components with a single frequency and with a triple frequency. The latter will, however, not be taken into account, since the focus of this work is on the tidally averaged transport, where the triple frequency is unnecessary, when no higher-order velocity terms are considered.

Taking all these contributions together, finally, gives the following expression for the sediment concentration

$$C = C_{M_0} + C_{M_4} \cos(2t - \xi_{M_4}) + \epsilon C_{M_2}^{int} \cos(t - \xi_{M_2}^{int})$$
$$+ \overline{\gamma} C_{M_2}^{ext} \cos(t - \xi_{M_2}^{ext}) + \text{h.o.t.}, \quad (2.24)$$

where C_{M_0}, $C_{M_2}^{int}$, $C_{M_2}^{ext}$ and C_{M_4} are the amplitudes of the tidally averaged, the semidiurnal (due to internally generated and externally prescribed overtides, respectively) and the quarter diurnal constituents of the sediment concentration respectively, while $\xi_{M_2}^{int}$, $\xi_{M_2}^{ext}$ and ξ_{M_4} are the phases of the respective constituents. To simplify notations in the remainder of this paper, the following notations are used for the semidiurnal tidal constituent of the water level (A_{M_2}, θ_{M_2}), the longitudinal velocity (U_{M_2}, ϕ_{M_2}) and the lateral velocity (V_{M_2}, φ_{M_2}). Similar notations are adopted for the M_0 and M_4 components. From this, the depth-integrated sediment transport can be expressed in terms of

amplitudes and phases of the velocities and the sediment concentration,

$$q_u = a \left\langle \epsilon u C - \mu \frac{\partial C}{\partial x} - \mu \Lambda \beta C \frac{\partial h}{\partial x} \right\rangle$$

$$= \underbrace{a\epsilon^2 U_{M_0} C_{M_0}}_{q_{u,\text{adv}}^{M_0}} + \underbrace{\frac{a\epsilon^2}{2} U_{M_2} C_{M_2}^{\text{int}} \cos\left(\phi_{M_2} - \xi_{M_2}^{\text{int}}\right)}_{q_{u,\text{adv}}^{M_2,\text{int}}}$$

$$+ \underbrace{\frac{a\epsilon^2}{2} U_{M_4}^{\text{int}} C_{M_4} \cos\left(\phi_{M_4}^{\text{int}} - \xi_{M_4}\right)}_{q_{u,\text{adv}}^{M_4,\text{int}}}$$

$$+ \underbrace{\frac{a\epsilon\overline{\gamma}}{2} U_{M_2} C_{M_2}^{\text{ext}} \cos\left(\phi_{M_2} - \xi_{M_2}^{\text{ext}}\right)}_{q_{u,\text{adv}}^{M_2,\text{ext}}}$$

$$+ \underbrace{\frac{a\epsilon\overline{\gamma}}{2} U_{M_4}^{\text{ext}} C_{M_4} \cos\left(\phi_{M_4}^{\text{ext}} - \xi_{M_4}\right)}_{q_{u,\text{adv}}^{M_4,\text{ext}}}$$

$$- \underbrace{a\mu \frac{\partial C_{M_0}}{\partial x}}_{q_{u,\text{diff}}^{M_0}} - \underbrace{a\mu\Lambda \frac{\partial h}{\partial x} \beta_{M_0} C_{M_0}}_{q_{u,\text{topo}}^{M_0}}$$

$$- \underbrace{\frac{a\mu\Lambda\epsilon^2}{2} \beta_{M_2} C_{M_2}^{\text{int}} \cos(\theta_{M_2} - \xi_{M_2}^{\text{int}}) \frac{\partial h}{\partial x}}_{q_{u,\text{topo}}^{M_2,\text{int}}}$$

$$- \underbrace{\frac{a\mu\Lambda\epsilon\overline{\gamma}}{2} \beta_{M_2} C_{M_2}^{\text{ext}} \cos(\theta_{M_2} - \xi_{M_2}^{\text{ext}}) \frac{\partial h}{\partial x}}_{q_{u,\text{topo}}^{M_2,\text{ext}}} \quad (2.24)$$

and analogously for q_v, with $\beta_{M_0} = \beta^{00}$ (see Eq. 2.15) and $\beta_{M_2} = \frac{-\Lambda A_{M_2} e^{-\Lambda(1-h)}}{(1-e^{-\Lambda(1-h)})^2}$. In Appendix A, the connection is clarified between the sediment transport used here and that when only tidal asymmetry, related to the velocity amplitudes, is considered.

2.5.2 Numerical solution method

The equations are spatially discretised using the Finite Element Method (FEM). More precisely, the Galerkin method will be applied on a grid of triangular elements. Piecewise quadratic interpolation functions (P2 elements) are used for the leading order system of Eqs. 2.16a–2.17a and linear interpolation functions (P1 elements) for the first order systems Eqs. 2.18a–2.19a and 2.20a–2.21a. The degree of the interpolation functions for the leading order system of equations should be at least one degree higher than for the first order system of equations, because the derivatives of the leading order variables are used as forcing terms in the first order system of equations. For the implementation of the FEM, the FEniCS software is used (Alnæs et al. 2015).

The computational grid was produced using the Gmsh module (Geuzaine and Remacle 2009) and consists of two parts: a part covering the physical domain and an extension to avoid oscillatory behaviour at the open boundary, due to the combination of a laterally uniform boundary condition and a laterally varying bottom profile (Boelens et al. 2018).

In the remainder of this paper, structured triangular grids are used with 60 vertices in the lateral direction and 1497 in the longitudinal direction (Δx and Δy range from ca. 100 m to ca. 1 m), resulting in 89820 nodes (including the domain extension).

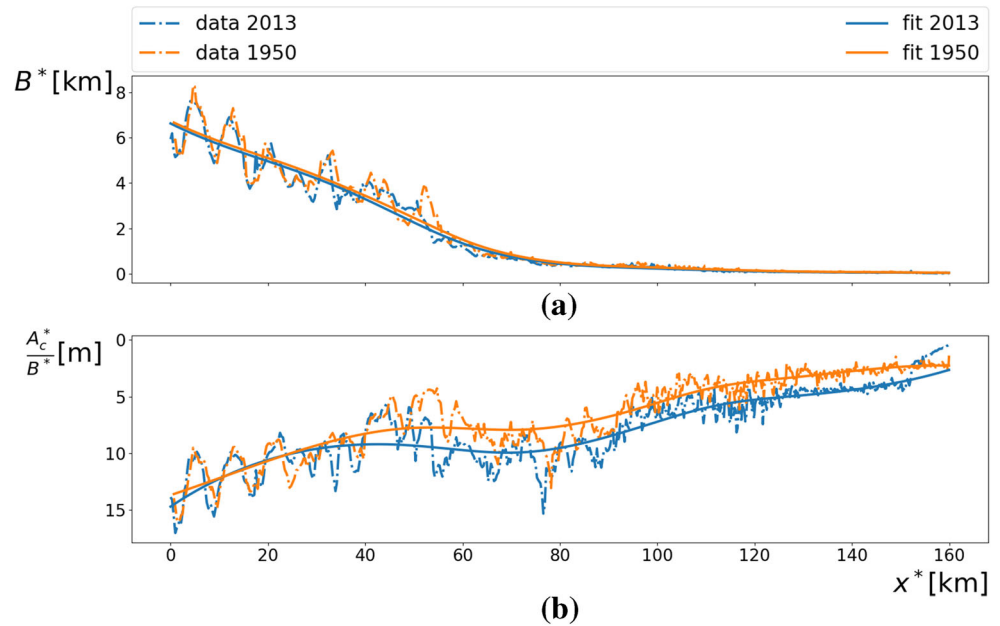## 3 Results

3.1 Model geometry

The model is applied to the main branch of the Scheldt estuary from Vlissingen to Gentbrugge, which has a length of 160 km. Based on historical (ca. 1950) and recent (2013) bathymetric data (Coen et al. 2015), a tidally averaged width profile, as well as a tidally and width-averaged depth, is determined. The data comprise yearly averaged values of the width and the wetted cross-section at high and at low water along the estuary. Taking the average of the width at high and low water, we get the tidally averaged width variation $B^*(x^*)$. Similarly, the average of the wetted cross-section at high and low water is denoted as $A_c^*(x^*)$. The tidally and width-averaged depth is then defined as $\overline{H^*} - h_{ave}^* = A_c^*/B^*$, where $\overline{H^*}$ is the tidally and width-averaged water depth at the open boundary and $h_{ave}^*(x^*)$ the width-averaged bed level, which is zero at the open boundary. The tidally averaged width and depth profiles are presented as the dash-dotted lines in Fig. 3 a and b, respectively. In the idealised modelling approach, we apply the Savitzky-Golay filter on the data to spatially smooth the varying geometry and bathymetry. The smoothed data are then fitted using smooth splines, presented as the full lines in Fig. 3.

The bottom profile defined by Eq. 1, depends on three parameters: d_1^*, d_2^* and α_h^*. To assure that no drying occurs, the values of $d_1^*(x^*)$ are chosen equal to half the tidal range. The values of d_2^* and α_h^* are determined by two additional conditions. As the first condition, the tidally averaged cross-sectional area is fitted to the data:

$$B^* \left(\overline{H^*} - h_{ave}^*\right) = \int_{-B^*/2}^{B^*/2} \left[d_1^* + d_2^* e^{-(y^*/\alpha_h^*)^2}\right] dy^*$$

$$\Rightarrow d_2^* = \frac{B^* \left(\overline{H^*} - h_{ave}^* - d_1^*\right)}{\alpha_h^* \sqrt{\pi} \, \text{erf}\left(\frac{B^*}{2\alpha_h^*}\right)}, \quad (3.1)$$

where erf(.) denotes the error function and the variables B^*, h_{ave}^*, d_1^*, d_2^* and α_h^* all depend on x^*.

Fig. 3 *Top panel:* Fitted curves to the tidally averaged width variation. *Bottom panel:* Fitted curves to the tidally and width-averaged depth (below tidally averaged water level). Data (dash-dotted lines) and fits (full lines) for the Scheldt estuary in 1950 are given in orange and for 2013 in blue

(a)

(b)

The Western Scheldt (the part of the estuary between Vlissingen and the Dutch-Belgian border, see Fig. 1) can be subdivided into a series of macro-cells, each consisting of meandering ebb channels, straight flood channels and intertidal sandbars between the channels. Generally, the main ebb channels are deepest and form the navigation route to the Port of Antwerp, while the main flood channels are shallower (Van Rijn 2013). Since the velocity field is highly correlated with the depth variations (Li and Valle-Levinson 1999) and the planform of the channels, this complex topo-bathymetry leads to a large spatial variation in flow velocities and therefore also sediment transport patterns.

The schematisation of our model is not able to reproduce this complexity, but it is aimed to find an optimal agreement with reality. Therefore, as a second condition, we fit the

model to reproduce the hypsometric curves of the total volume as a function of the vertical water level. Based on data from Beullens et al. (2017), the estuary is divided in five main sections and for each section, we have fitted a constant α_h^* to the corresponding hypsometric curve, using condition Eq. 3.1. Afterwards, we approximated these piecewise constant values for α_h^* with a continuous function (hyperbolic tangent), using a least squares analysis. The values for $\alpha_h^*(x^*)$ and $d_2^*(x^*)$, obtained in this way, are validated, using the hypsometric curves for the entire Western Scheldt, from Kuijper and Lescinski (2013). These curves are compared with the hypsometric curves, composed with the present geometry, both for the surface area and for the total volume in function of the vertical level, resulting in a good qualitative agreement (see Fig. 4).

Fig. 4 Hypsometric curves of the surface area and the total volume under a certain vertical level with respect to the tidally averaged water level H
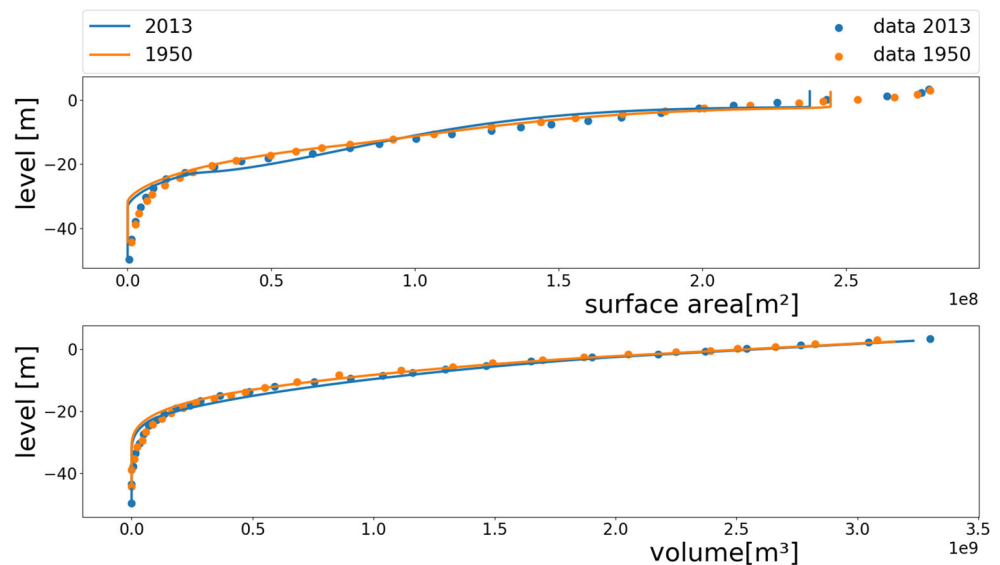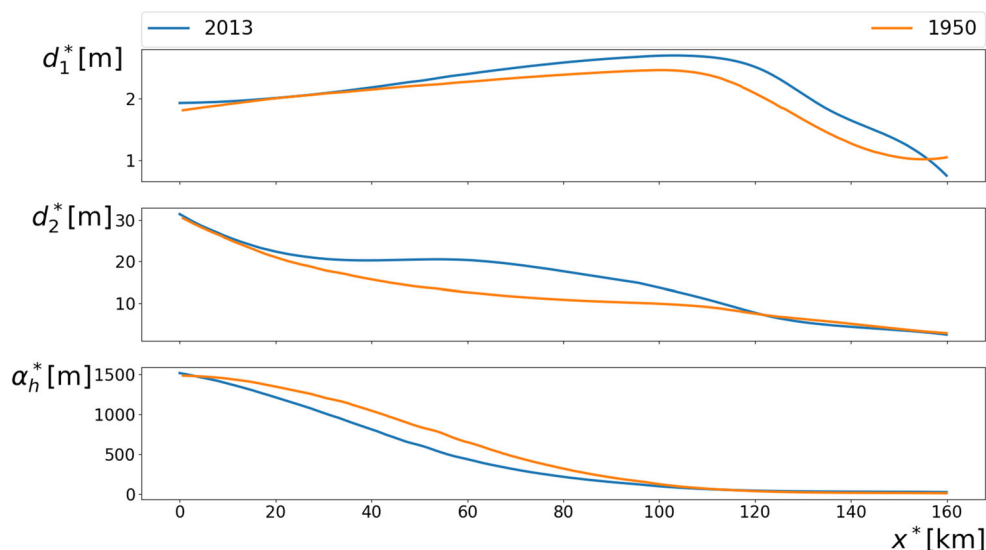
Fig. 5 Variation of the geometric parameters d_1^*, d_2^* and α_h^*, determining the shape of the bathymetry

The variation of d_1^*, d_2^* and α_h^* along the estuary is shown in Fig. 5. Some examples of the cross-sectional shape along the estuary, together with the variation of the cross-sectional area at low water (orange lines), high water (blue lines) and tidally averaged water level (green lines), are given in Fig. 6, showing a good agreement with observations, both at high and low water. The colour of the small vertical lines at the top of the bottom figures in Fig. 6 indicates the location of the cross-section with the same colour in the top figures.
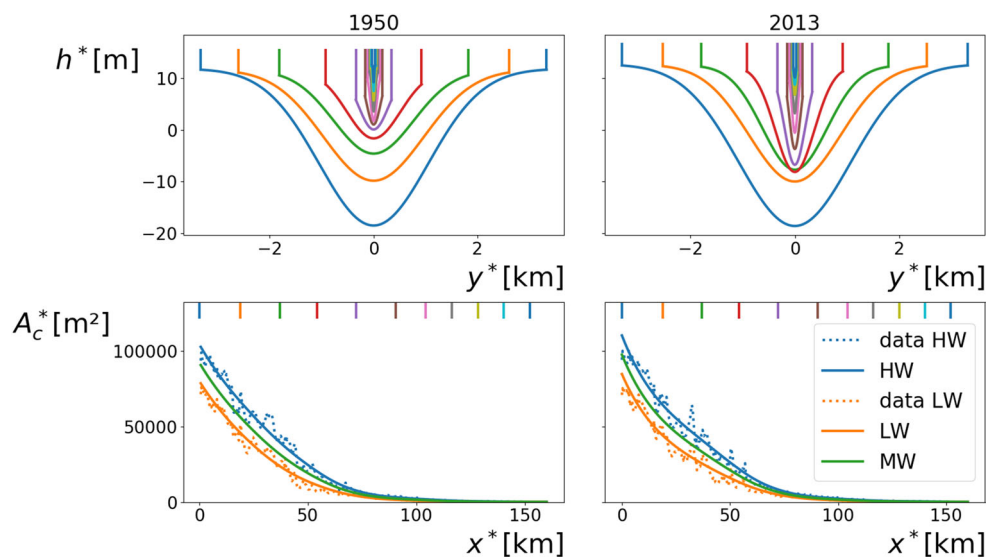
3.2 Model validation

When using an exploratory model, no quantitatively accurate model results may be expected, when compared with observations. Exploratory models do not aim at such an

accurate quantitative comparison, but instead at *qualitatively* capturing and explaining trends in tidal amplitudes, sediment transport, etc, related to e.g. changes in forcing conditions in the system under investigation.

In view of this, it is not our aim to represent the sediment transport throughout the estuary as accurately as possible, but to investigate the changes in the sediment transport due to past and future changes in the environmental factors. Since we apply our exploratory model to the Scheldt estuary as a test case, we calibrate our model such that it qualitatively captures the main tidal properties (propagation speed, amplitudes, ...), resulting in an adequate representaton of the present-day sediment transport. This allows us to qualitatively assess the sensitivity in the sediment transport due historic changes in the Scheldt, and study trends due to future changes.

Fig. 6 *Top panels:* Cross-sectional shape of the bed at various locations along the estuary, given by the coloured vertical lines on top of the bottom figures. *Bottom panels:* Variation of the cross-sectional area at low water (LW), high water (HW) and tidally averaged (MW) along the estuary

The model is calibrated by choosing the friction parameter r, such that the difference between the calculated and observed M_2 and M_4 amplitudes and phases of the water level and the cross-sectionally averaged velocity is minimised. This friction parameter is then used unalteredly for the simulations regarding the historical situation (ca. 1950) as well.

The observed values (dots in Fig. 7) are taken from Brouwer et al. (2017) and are based upon processing by Nnafie et al. (2016) of recent measurements in the Scheldt Estuary, i.e. water level data from the tidal gauge network and velocities measured throughout a tidal cycle along eleven different transects.

Figure 7b shows that the water level M_2 and M_4 phases of the recent situation compare quite well with the data (full lines compared with dots). This means that the propagation of the tidal wave is captured accurately by the model. In Fig. 7a, it is shown that the M_2 amplitude overestimates the observed amplitudes upstream of 100 km, while the M_4 amplitude is overestimated throughout the entire estuary. The velocity measurements are harder to perform and exhibit much more variation along the cross-section, especially in the Western Scheldt (Fig. 7c). Consequently, the measured velocities show more variance. There is a large discrepancy between the measured data and the model results for the M_2 velocity amplitude in the most seaward part. This can (partly) be explained by the schematisation of the local bathymetry, as discussed in the previous section.

However, the qualitative behaviour of the M_2 and especially the M_4 velocity amplitudes is captured by the model.

As stated earlier, the historical simulations are not calibrated explicitly to data. However, Fig. 7 shows that the M_2 amplitude of the water level is lower in the historical case and the peak amplitude is situated more seaward. This is in accordance with measurements of the tidal range as shown in e.g. Taverniers et al. (2013). Furthermore, the phase of the semi- and quarter diurnal constituents of the water level has decreased over the past century, indicating a faster propagation of the tidal wave. These results are consistent with results obtained, using a simulation model (Van der Werf and Briere 2013).

3.3 Comparison of sandy sediment concentration and transport in the recent and the historical situation

In this section, we will compare two cases based on a historical (ca. 1950) and a more recent (2013) situation in the Scheldt estuary (Barneveld et al. 2018). This will provide insight in the response of the tidally averaged transport of fine sand to changing conditions in the estuary over the years. The smoothed planview geometries (see Fig. 3) are very similar for both cases. The bathymetry, however, differs significantly. Furthermore, the mean sea level has increased in the recent situation, compared with the historical one. We should remark that the difference in mean
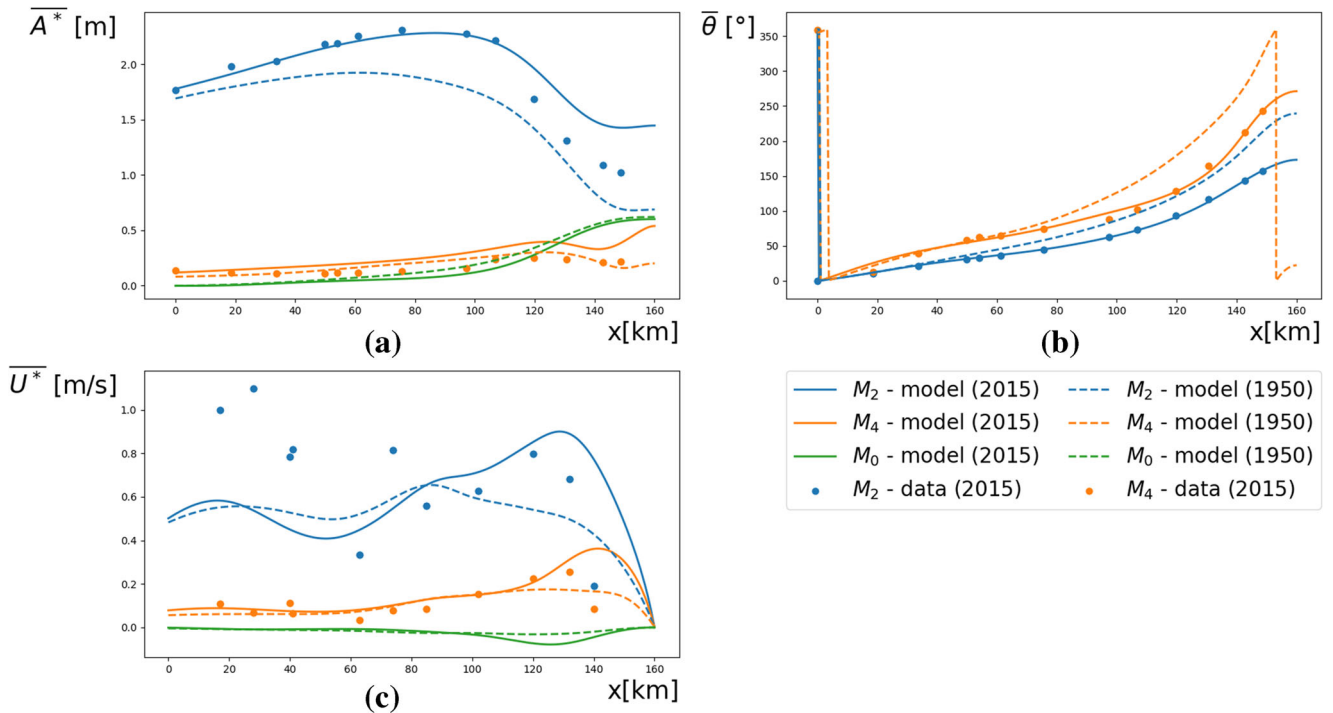

Fig. 7 Measurement data (dots) and model results for the recent (full lines) and historical (dashed lines) situation in the Scheldt estuary for the M_2 (blue) and M_4 (orange) amplitudes and phases and the tidally averaged components (green) of the water level amplitudes (panel **a**) and phases (panel **b**) and the cross-sectionally averaged velocities (panel **c**)

sea level $\overline{H^*}$ as given in Table 1 is the sum of the deepening of the cross-section and the actual sea level rise at the mouth of the estuary; the latter has only increased ca. 0.22 m over the past century (Van Braeckel et al. 2007). Finally, the tidal forcing at the seaward side has changed significantly as well: the semidiurnal amplitude $\overline{A^*_{M_2}}$ has increased from 1.68 to 1.77 m, the quarter diurnal amplitude $\overline{A^*_{M_4}}$ has increased from 0.11 to 0.14 m and the relative phase between the semi- and quarter diurnal tidal constituents $\overline{\theta_{\text{rel}}} = 2\overline{\theta_{M_2}} - \overline{\theta_{M_4}}$ has changed from -5.4 to $-1.3°$ (see Table 1). In all simulations, the same friction parameter has been applied. Consequently, the differences between the simulations are due to changes in the bathymetry, mean sea level or tidal forcing. In the next section, the influence of each of these individual parameters on the tidally averaged sediment transport will be studied in more depth.

The suspended sediment concentration (SSC) and the width-integrated, tidally averaged sand transport are shown in Fig. 8a and b respectively. Here the width-integrated, tidally averaged sand transport is defined as

$$\widehat{q_u} = \int_{B^*} q_u^* \, \mathrm{d}y^* \tag{3.2}$$

In the remainder of this paper, we will refer to $\widehat{q_u}$ as the total tidally averaged sand transport, where, in this case, "total" means integrated over the entire cross-section.

For both years, the SSC has a peak value around 130 km (see Fig. 8a). The location of the peak has not shifted much between the historical (dashed line) and the recent (full line) situation, but the magnitude of the peak concentration has doubled. Measurement data, presented in Maris and Meire (2016), show a peak value around 110 km of $0.16\,\text{kg m}^{-3}$ of depth-averaged SSC in summer conditions (low river discharge), averaged over the period 2009–2015. It should be noted that these data pertain to the total SSC, not only sand, and that there is a large annual variability. Nevertheless, the gross longitudinal variation and the order of magnitude of the depth-averaged SSC, presented in Fig. 8a, agree with the data. The more downstream location of the peak concentration in the data, compared with the present simulation results, can (partially) be explained by the absence of a freshwater discharge in the current model. Also in Chen et al. (2005), the sediment concentration is stated to be higher in the landward part of the estuary than in the seaward part and their measured concentrations are of the same order of magnitude as our results. Moreover, according to Chen et al. (2005), measured time series have shown an increase in the sand fraction of the sediment concentration over the period 1991–2000, especially around the peak concentration, which is in accordance with the results, shown in Fig. 8a.

The total tidally averaged sand transport is shown in Fig. 8b. Negative values indicate that sediment is

(a) SSC$[\text{kg m}^{-3}]$

(b) $\widehat{q_u}\,[\text{kg s}^{-1}]$

(c) $q_u^*[\text{kg m}^{-1}\,\text{s}^{-1}]$ (1950)

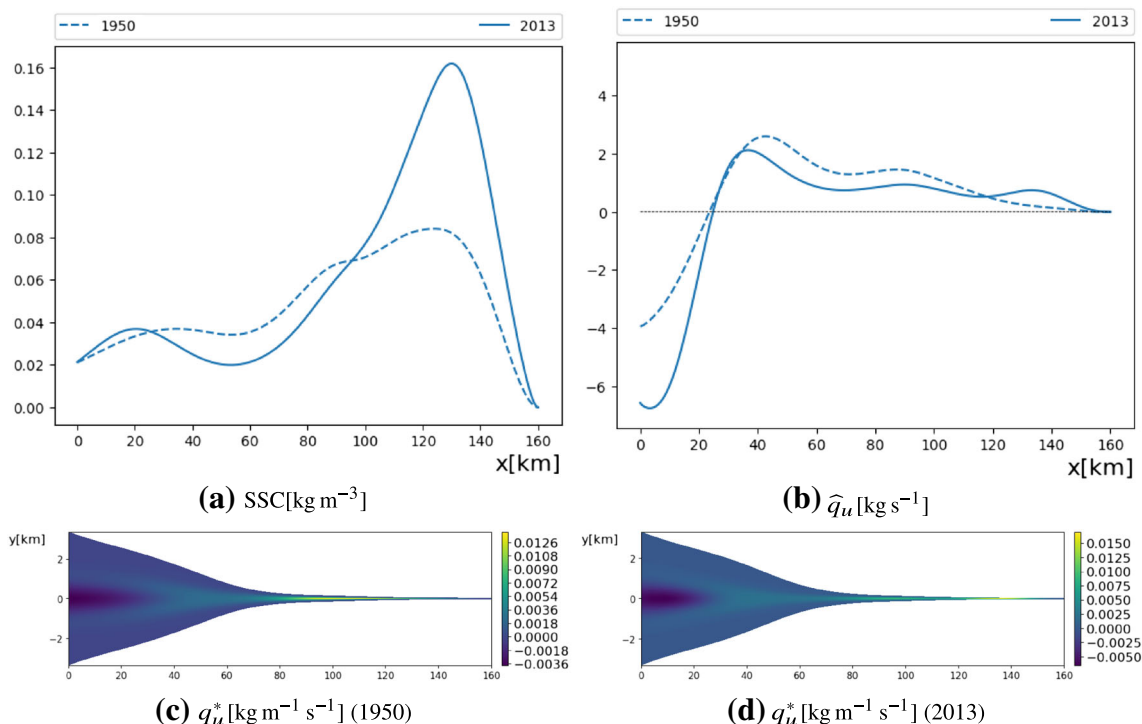**(d)** $q_u^*[\text{kg m}^{-1}\,\text{s}^{-1}]$ (2013)

Fig. 8 Depth-averaged suspended sediment concentration (**a**) and the width-integrated, tidally averaged sediment transport (**b**) for the historical (dashed lines) and the recent (full lines) situation. **c, d** Spatial variation of the tidally averaged sediment transport in the historical and the recent situation, respectively

transported seaward (export) and positive values indicate sediment is transported landward (import). This means that sediment is transported seaward in the first 20 km of the estuary, while upstream of 20 km, the sediment is transported landward. Consequently, there is a divergence point around $x = 20$ km, i.e. a point where sediment at either side is being transported away from that point and the estuary tends to deepen. This effect is more pronounced in the recent situation (2013), since both the maximum seaward and maximum landward transport are closer to the divergence point, leading to a steeper gradient in the sand transport. Appendix A clarifies the importance of using the full Eq. 2.24, since tidal velocity amplitude asymmetry suggests that sediment would be transported landward along the entire channel (see Fig. 12).

Furthermore, the maximum seaward sand transport has increased compared with the historical situation. This is also observed in Fig. 8c and d that show the two-dimensional pattern of the tidally averaged sand transport for the historical and the recent situation, respectively. Moreover, Fig. 8c and d show a landward shift and an increase in the maximum landward sediment transport. The increase of this local maximum is due to the higher amplitudes of the velocity constituents in the landward part of the estuary (see Fig. 7c).

The total tidally averaged sand transported in the (Western) Scheldt has been calculated, using a (Delft3D) simulation model by Van der Werf and Briere (2013). They also find a seaward transport close to the open boundary, which decreases along the estuary and eventually changes into a small landward transport. Furthermore, they find an increase over the years in the net sand export at the open boundary. These findings are qualitatively in accordance with Fig. 8b. Finally, in Cleveringa (2013), the total tidally averaged sand transport is estimated, based on differential maps of the bathymetry. They find a seaward sand transport near the seaward boundary and landward sand transport more upstream, which is again in accordance with Fig. 8b. Moreover, their results show an estimated net sand export through the seaward boundary of 0.52×10^6 m^3/year. Our model result gives a net sand export of ca. 6 kg/s. To convert from kilograms of matter in suspension to cubic metres of bed material, we calculate the net sand export over 1 year and divide it by $(1-p)\rho_s$, where $p = 0.4$ is the bed porosity and $\rho_s = 2650$ kg/m^3 is the density of sand. This gives a sand export of 0.12×10^6 m^3/year, which is of the same order of magnitude as the result from Cleveringa (2013).

We must note here, however, that there is quite some uncertainty in our model results concerning the net sand transport at the seaward boundary, due to the schematisation of the bathymetry and the discrepancy in the M_2-velocity amplitude in the seaward part of the estuary. Moreover, there is also some uncertainty in (the sign and magnitude of) the

net sand transport at the seaward boundary as derived from differential bathymetry maps. Other authors than Cleveringa (2013), such as Barneveld et al. (2018), found a net import of sand.

In Fig. 9, the different contributions to the tidally averaged sediment transport, given in Eq. 2.24, are depicted. The advective contributions are displayed in Fig. 9a. The advective contributions due to internally generated overtides ($\widehat{q}_{u,\mathrm{adv}}^{M_2,\mathrm{int}}$ and $\widehat{q}_{u,\mathrm{adv}}^{M_4,\mathrm{int}}$) are positive and the dominant contributions to the total tidally averaged sand transport upstream of 20 km. Close to the seaward boundary, the advective contributions due to externally prescribed overtides ($\widehat{q}_{u,\mathrm{adv}}^{M_2,\mathrm{ext}}$ and $\widehat{q}_{u,\mathrm{adv}}^{M_4,\mathrm{ext}}$) result in a seaward sand transport, together with the advective contribution due to residual components ($\widehat{q}_{u,\mathrm{adv}}^{M_0}$) and the topographically induced contribution ($\widehat{q}_{u,\mathrm{topo}}^{M_0}$). The other topographically induced contributions ($\widehat{q}_{u,\mathrm{topo}}^{M_2,\mathrm{int}}$ and $\widehat{q}_{u,\mathrm{topo}}^{M_2,\mathrm{ext}}$) are much smaller and are therefore not shown here. Around the divergence point, the total tidally averaged sand transport (Fig. 8b) is zero, even though all advective contributions attain their extreme value. Due to a decrease in the absolute value of the tidally averaged velocity in the seaward part of the estuary, $\widehat{q}_{u,\mathrm{adv}}^{M_0}$ has decreased as well (in absolute value). In contrast, all other contributions to the tidally averaged sand transport and especially their extreme values have grown stronger in the recent situation (2013) compared with the historical situation (1950). This is mainly due to an increase in the tidally varying constituents of the suspended sediment concentration, as the velocity constituents show no clear increase in the seaward part of the estuary (see Fig. 7c). The changes in the different contributions to $\widehat{q}_u$ will be explained in further detail in the discussion section.

4 Discussion

4.1 Historical evolution of the tidally averaged sand transport

In the previous sections, the tidally averaged sand transport was described for a historical (ca. 1950) and a recent (2013) situation in the main branch of the Scheldt estuary.

In this section, the specific influence on the total tidally averaged sand transport of the deepening of the estuary on the one hand and the changing tidal forcing (semidiurnal amplitude, quarter diurnal amplitude and relative phase) on the other hand, will be discussed. To this end, several simulations have been performed, which are summarised in Table 2. The results are shown in Fig. 10.

The recent situation (2013) is depicted with full blue lines, while the historical situation (ca. 1950) is depicted with dashed blue lines. In the other simulations, one or
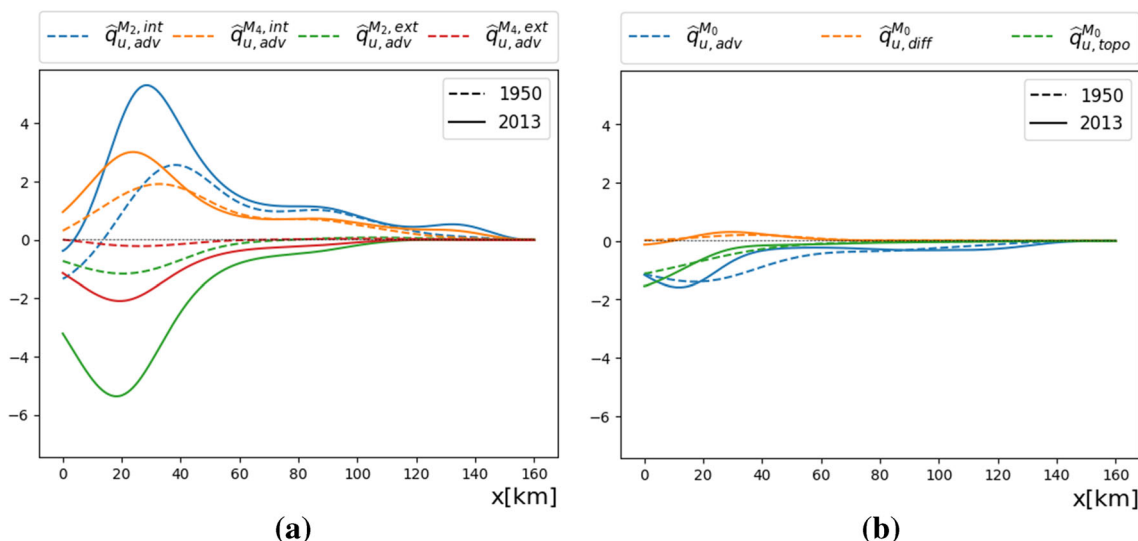
Fig. 9 Different contributions to the total tidally averaged sand transport [kg s^{-1}] for the historical (dashed lines) and the recent (full lines) situation

more parameter values of the recent situation have been altered to parameter values of the historical situation (see Table 2). Thus, the influence of each of these separate changes on the total tidally averaged sand transport and its various contributions can be studied in isolation. Note that the diffusive and the topographically induced contributions are not depicted here, since the corresponding differences between the historical and the recent situation are small.

Changing the quarter diurnal water level amplitude that is prescribed at the entrance (orange dotted lines) or the relative phase (orange dashed lines) only affects the advective contributions to the total tidally averaged sand transport due to externally prescribed overtides $\widehat{q}_{u,\mathrm{adv}}^{M_2,\mathrm{ext}}$ (Fig. 10a) and $\widehat{q}_{u,\mathrm{adv}}^{M_4,\mathrm{ext}}$ (Fig. 10b). Changes in the M_4-velocity (see Fig. 7c) and thus in $\widehat{q}_{u,\mathrm{adv}}^{M_4,\mathrm{ext}}$ are moderate, but the concentration constituent due to the external M_4 tide decreases significantly (not shown here). Consequently, for $\widehat{q}_{u,\mathrm{adv}}^{M_2,\mathrm{ext}}$, the seaward transport strongly decreases, compared with the recent situation (blue full lines), when the quarter-diurnal amplitude or phase decreases. This implies that

the landward directed contributions $\widehat{q}_{u,\mathrm{adv}}^{M_2,\mathrm{int}}$ (Fig. 10c) and $\widehat{q}_{u,\mathrm{adv}}^{M_4,\mathrm{int}}$ (Fig. 10d) to $\widehat{q}_u$ (Fig. 10d) become more important in a relative way, leading to a seaward shift of the divergence point, a weaker seaward transport and a higher maximum landward transport.
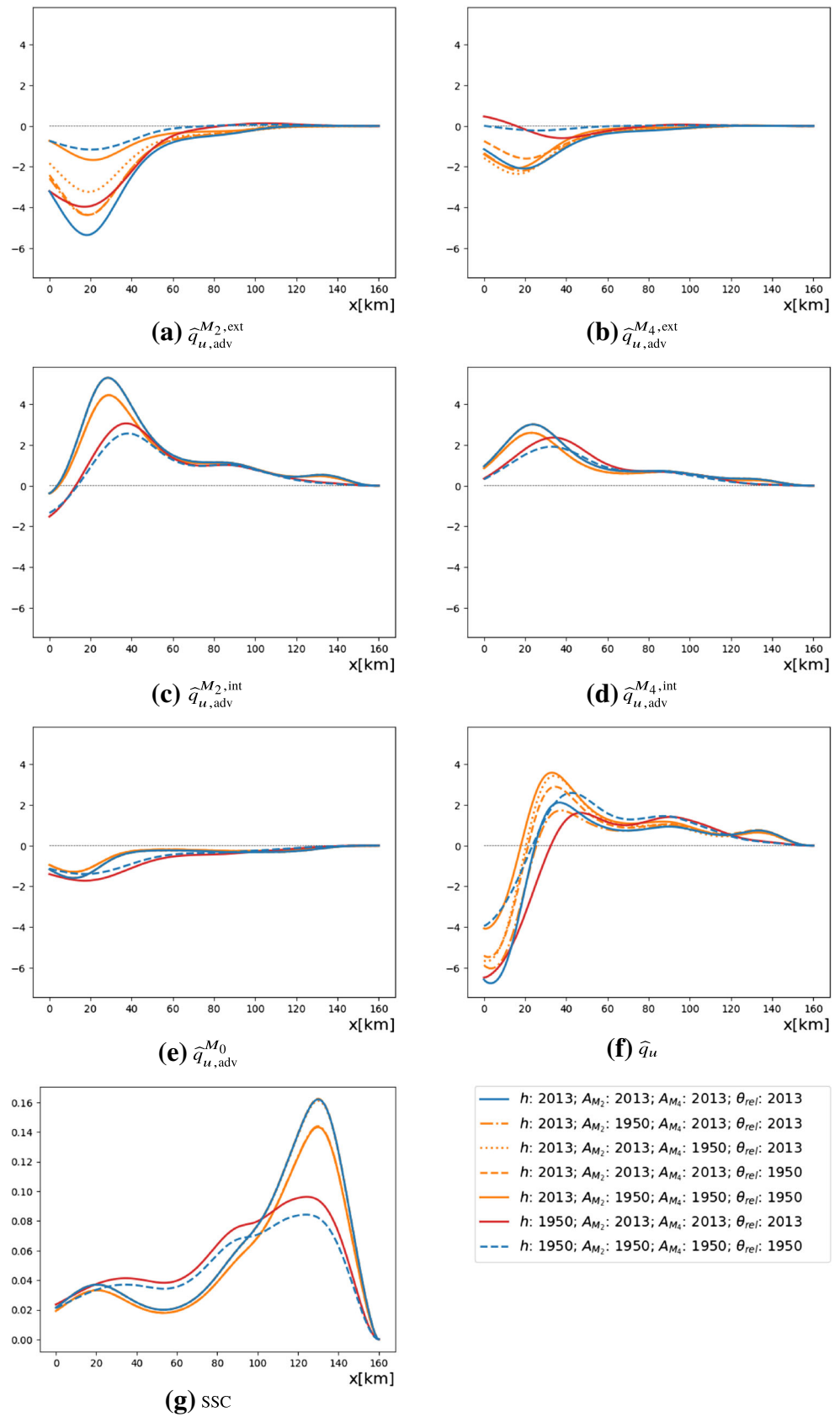
Decreasing the semidiurnal water level amplitude (orange dash-dotted lines) leads to a moderate decrease in absolute value of all velocity and concentration constituents, as well as all contributions to the tidally averaged sand transport. This leads to both a weaker seaward and landward transport. Note that orange dash-dotted lines and the orange full lines coincide in Fig. 10c to e, because these contributions do not depend on the quarter diurnal forcing at the entrance, which means they are completely determined by the changes in M_2.

Changing the complete tidal forcing (orange full lines) to the value of 1950 decreases all velocity and concentration constituents. Hence, all contributions to the transport are weakened, compared with the recent situation (blue full lines). However, not all tidal constituents and thus, not

Table 2 Summary of the different situations, depicted in Fig. 10, where one or more parameters have been changed (indicated in red), compared to the standard recent situation, shown in Fig. 9

Fig. 10		Parameters			
Color	Linestyle	Bathymetry	$\overline{A_{M_2}^*}$	$\overline{A_{M_4}^*}$	$\overline{\theta_{\mathrm{rel}}}$
blue	full	2013	1.77 m	0.14 m	$-1.3°$
blue	dashed	1950	1.68 m	0.11 m	$-5.4°$
orange	dotted	2013	1.77 m	0.11 m	$-1.3°$
orange	dashed	2013	1.77 m	0.14 m	$-5.4°$
orange	dash-dotted	2013	1.68 m	0.14 m	$-1.3°$
orange	full	2013	1.68 m	0.11,m	$-5.4°$
red	full	1950	1.77 m	0.14 m	$-1.3°$

Fig. 10 **a–e** A selection of the contributions to **f** the total tidally averaged sand transport [kg s^{-1}], and **g** the SSC [kg m^{-3}] for different simulations, as described in Table 2

(a) $\widehat{q}_{u,\mathrm{adv}}^{M_2,\mathrm{ext}}$

(b) $\widehat{q}_{u,\mathrm{adv}}^{M_4,\mathrm{ext}}$

(c) $\widehat{q}_{u,\mathrm{adv}}^{M_2,\mathrm{int}}$

(d) $\widehat{q}_{u,\mathrm{adv}}^{M_4,\mathrm{int}}$

(e) $\widehat{q}_{u,\mathrm{adv}}^{M_0}$

(f) $\widehat{q}_{u}$

(g) SSC

h: 2013; A_{M_2}: 2013; A_{M_4}: 2013; θ_{rel}: 2013
h: 2013; A_{M_2}: 1950; A_{M_4}: 2013; θ_{rel}: 2013
h: 2013; A_{M_2}: 2013; A_{M_4}: 1950; θ_{rel}: 2013
h: 2013; A_{M_2}: 2013; A_{M_4}: 2013; θ_{rel}: 1950
h: 2013; A_{M_2}: 1950; A_{M_4}: 1950; θ_{rel}: 1950
h: 1950; A_{M_2}: 2013; A_{M_4}: 2013; θ_{rel}: 2013
h: 1950; A_{M_2}: 1950; A_{M_4}: 1950; θ_{rel}: 1950

all contributions to the tidally averaged sand transport are weakened equally. Indeed, $\widehat{q}_{u,\mathrm{adv}}^{M_2,\mathrm{ext}}$ is much more sensitive to changes in the tidal forcing than the other components. This leads again to an increased relative importance of $\widehat{q}_{u,\mathrm{adv}}^{M_2,\mathrm{int}}$ and $\widehat{q}_{u,\mathrm{adv}}^{M_4,\mathrm{int}}$ and consequently to a seaward shift of the divergence point, a weaker seaward transport and a higher maximum in the landward transport (Fig. 10f).

A completely different picture arises, when we change the bathymetry (red full lines), compared with the recent situation (blue full lines). The phases of all the velocity and concentration constituents (not shown here) increase, meaning the horizontal tide will propagate slower through the estuary with the 1950 bathymetry. The velocity amplitudes show a clear decrease in the most landward part of the estuary (see Fig. 7c), leading to the vanishing of the second smaller maximum in landward transport, close to the landward boundary. The amplitudes of the concentration constituents (not shown here) have decreased throughout the estuary, so the maxima (in absolute value) of the advective contributions have decreased and shifted landward, as can be seen in Fig. 10a to d. Finally, the advective contribution due to interactions of residual velocities and concentrations has increased between 20 and 80 km (Fig. 10e), due to an increasing tidally averaged velocity constituent (in absolute value). The combined effect on the total tidally averaged sand transport (Fig. 10f) is a landward shift of the divergence point, a decrease and a landward shift of the maximum in the landward transport and the vanishing of the second smaller maximum in landward transport.

The changes in SSC (Fig. 10g) are mainly due to the changes in bathymetry. In leading order, SSC depends mainly on the tidally averaged constituent of the sediment concentration, which is forced by the semidiurnal velocity constituents. The tidal forcing only affects the magnitude of the semidiurnal velocity and thus of the (maximum) concentration, but does not strongly influence its along channel behaviour, contrary to the shape of the bed.

In summary, we can state that both the change in bathymetry and the change in tidal forcing strongly impact the total tidally averaged sand transport. However, these changes affect the tidal velocity and concentration constituents, and thus the contributions to the total tidally averaged sand transport, in different ways. Changes in tidal forcing mainly influence the export at the seaward boundary. An increase of the tidal amplitudes (orange full lines vs. blue full lines or blue dashed lines vs. full red lines) leads to stronger export at the seaward boundary, to a landward shift of the divergence point and to a decreased maximum landward transport. Bathymetric changes, on the other hand, have a negligible influence on the export. Deepening of the estuary (red full lines vs. blue full lines or blue dashed lines vs. orange full lines) leads to a seaward shift of the divergence point, an increase of the

maximum landward transport and the manifestation of the local maximum in the landward transport near the landward boundary. So changes in tidal forcing and bathymetry can result in opposite changes in the total tidally averaged sand transport, which results from a subtle balance between its various contributions.

4.2 Future evolution of the tidally averaged sand transport

In this section, we will present sensitivity studies by means of the calibrated model for the 2013-situation, performed against the background of future sea-level rise (SLR). We will consider a SLR of up to $+1\,\mathrm{m}$. A flood mitigation measure that receives quite some attention in light of projected SLR is the so-called managed retreat, where human made flood defences are being removed to give back land to the river. In Townend and Pethick (2002), a conceptual model is presented for both a scenario with managed retreat and with SLR in an unaltered estuary. Although several managed retreat projects have been established (or will be in the future) in the Scheldt estuary, we will assume in the following that the geometry does not change. According to Townend and Pethick (2002), an increase in the mean water level will increase the hydraulic depth of the channel and therefore the tendency for flood dominance. The enhanced import of sediment will then deposit in the shallow zones, which will increase in elevation, thereby reducing the storage volume of the estuary, which again favours ebb dominance (Friedrichs and Aubrey 1988). We will assume that characteristic response time of the estuary is of the same order as the rate of SLR, i.e. we assume that the shallow zones can keep up with the estimated SLR (Kirwan and Megonigal 2013). This means that to determine the bathymetry in light of SLR, we keep $d_1^*(x^*)$ and $\alpha_h^*(x^*)$ identical to the 2013-situation; $d_2^*(x^*)$ is then determined such that the cross-sectional area equals $B^*(\overline{H^*} - h_{ave}^*)$, where $\overline{H^*}$ is now the value of the 2013-situation augmented with the SLR.

Sea-level rise does not only modify the mean water levels, but also the tidal dynamics (Pickering et al. 2017). Notable increases in high tide levels occur in the southern part of the North Sea and these changes are generally proportional to SLR, as long as SLR remains smaller than 2 m (Idier et al. 2017). Since there is still quite some uncertainty on the response of the tidal components to SLR, depending o.a. on the coastal defence systems that may or may not be employed, we will assume a moderate and a more extreme scenario. Based on model results from Pickering et al. (2012), Ward et al. (2012), and Verlaan et al. (2015) and Idier et al. (2017), in the moderate scenario, $\overline{A_{M_2}*}$ will increase with 3% or ca. 5 cm, $\overline{A_{M_4}*}$ will decrease with 15% or ca. 2 cm and $\overline{\theta_{\mathrm{rel}}}$ will increase with 10° for a

SLR of $+1$ m. For more extreme scenarios, we have doubled these increases and decreases compared with the moderate scenario.

Figure 11 shows the total tidally averaged sand transport along the estuary (horizontal axis), for different values of SLR (vertical axis). The locations of the maximum seaward transport (dotted lines), the divergence point (dash-dotted lines) and the maximum landward transport (dashed lines) are indicated as well. Since the observed effects are similar

in the moderate and the more extreme scenarios, only the results for the more extreme scenarios are shown in Fig. 11.

Increasing the mean sea-level (Fig. 11a) and keeping the tidal forcing the same as in the 2013-situation lead to less friction and consequently to higher velocity amplitudes and higher suspended sediment concentrations. However, the positive and the negative contributions to the total tidally averaged sand transport get even more balanced, such that the total tidally averaged sand transport slightly decreases.
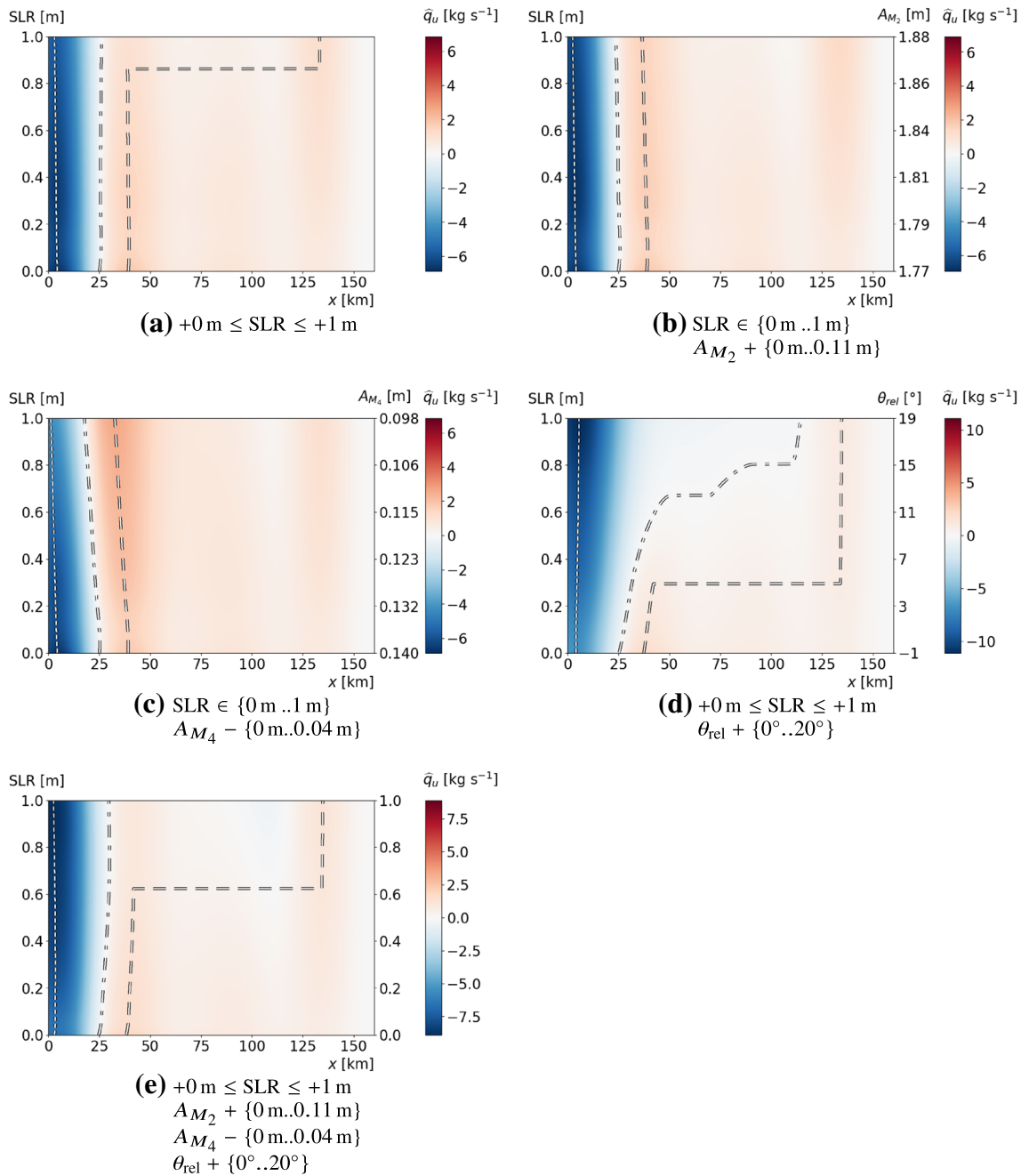

Fig. 11 The total tidally averaged sand transport $\widehat{q}_u$ along the estuary (x-axis), for different values of SLR (y-axis). The tidal forcing is varied in different ways, as explained in the subcaptions. The locations of the

maximum seaward transport (dotted lines), the divergence point (dash-dotted lines) and the maximum landward transport (dashed lines) are indicated as well

Both the maximum seaward transport (around 5 km) and the maximum landward transport (around 40 km) slightly decrease in absolute value with rising sea-level. The smaller maximum in landward transport, close to the landward boundary, on the other hand, increases with increased sea-level, such that around a SLR of 0.85 m, the local maximum in the landward transport, close to the landward boundary, becomes larger than the local maximum around 40 km. This is because the higher velocities in the landward part of the estuary are mainly due to the M_2 and the internally generated M_4 constituents. Therefore, the increased positive contributions are not balanced by the negative contributions due to externally prescribed overtides.

In Fig. 11b, sea-level has been changed together with M_2-amplitude (which varies linearly with SLR, up to 6% for SLR=+1 m). Where the increase in SLR resulted in a decrease in the landward transport maximum around 40 km (see Fig. 11a), this effect is not present when the M_2-amplitude is increased as well. From this, we conclude that the increased semidiurnal forcing slightly changes the balance between the different contributions in favour of the positive contributions. This implies that the landward transport maximum around 40 km remains larger than the secondary landward transport maximum, close to the landward boundary, for all scenarios depicted in this figure.

The M_4-amplitude has been varied linearly with SLR, up to -30% for SLR=+1 m, as depicted in Fig. 11c. This obviously leads to a decrease in the seaward directed transport terms, associated with the externally prescribed overtides ($\widehat{q}_{u,\mathrm{adv}}^{M_2,\mathrm{ext}}$ and $\widehat{q}_{u,\mathrm{adv}}^{M_4,\mathrm{ext}}$). Since the other contributions remain unaffected, the total tidally averaged sand transport exhibits a decrease in the (maximum) seaward transport and an increase in the (maximum) landward transport. The latter implies again that the landward transport maximum around 40 km remains larger than the secondary landward transport maximum, close to the landward boundary. Furthermore, the divergence point and the maximum landward transport are shifted seaward.

Subsequently, the relative phase, ranging from $-1°$ to $+19°$, has been altered linearly along with SLR in Fig. 11d. An increase in the relative phase of the water level constituents at the open boundary results in modified phases of the externally prescribed overtides of the tidal currents ($\phi_{M_4}^{\mathrm{ext}}$) and the suspended concentration ($\xi_{M_2}^{\mathrm{ext}}$). Subsequently, the associated changes in the phase difference between the velocity and the suspended concentration (see Eq. 2.24) result in stronger (negative) tidal contributions due to externally prescribed overtides ($\widehat{q}_{u,\mathrm{adv}}^{M_2,\mathrm{ext}}$ and $\widehat{q}_{u,\mathrm{adv}}^{M_4,\mathrm{ext}}$). This leads to a strong increase in the maximum seaward transport, while the maximum landward transport around 40 km completely disappears for SLR $\gtrsim$ 0.3 m, such that the only maximum in landward transport is situated near the landward boundary. Since the balance between the

increased negative contributions and the unaffected positive contributions has completely altered, the divergence point is shifted landward and the landward transport is very small up until ±110 km for a SLR between 0.3 and 0.7 m. Further increasing SLR and the relative phase enhances these effects and the total tidally averaged sediment transport even remains slightly negative up until the divergence point at ±110 km, for $\theta_{\mathrm{rel}} \gtrsim 15°$.

Finally, in Fig. 11e, sea-level has been changed, together with the complete tidal forcing. Interestingly, the effect of the tidal forcing seems rather limited. In comparison with Fig. 11a, there is an increase in the maximum seaward transport with SLR and a faster decrease of the maximum landward transport around 40 km, such that the secondary maximum in landward transport, close to the landward boundary, becomes larger already at a smaller SLR. It appears that the decrease of the M_4-amplitude and the increase of the relative phase, largely cancel each other out, since they both mainly affect the contributions $\widehat{q}_{u,\mathrm{adv}}^{M_2,\mathrm{ext}}$ and $\widehat{q}_{u,\mathrm{adv}}^{M_4,\mathrm{ext}}$, but in opposite ways. A hypothetical increase of the M_4-amplitude, together with an increase in the relative phase, would therefore lead to a strongly different behaviour of the total tidally averaged sand transport (not shown here).

These sensitivity studies give an overview of how the total tidally averaged sand transport will change under SLR, with various possibilities for the corresponding changes in tidal forcing. For the scenarios that were discussed in this section, changes in amplitudes or phases of the tidal constituents, due to SLR, can each have a big effect on the total tidally averaged sand transport. However, the changes in the different tidal constituents largely cancel each other out, such that the changes in mean sea-level become dominant. Generally, slight changes in the environmental conditions can have a large impact on the total tidally averaged sand transport, so it is crucial to have a good estimate of the response of the tidal signal to global SLR, in order to make accurate predictions about the transport of sandy sediments.

5 Conclusions

The exploratory depth-averaged model, developed in Boelens et al. (2018), has been extended by replacing the simple analytical approximation for the sediment transport with a more sophisticated approach, based on solving an advection-diffusion equation for the depth-integrated suspended sediment concentration. The model has been utilised to study a testcase, namely the historical development (ca. 1950–2013) of the tidally averaged transport of sandy sediments in the main branch of the (schematised) Scheldt estuary, as well as a future prediction, considering +1 m of SLR. The model uses the finite element method to

spatially discretise the equations, which are then solved in the frequency domain. This modelling approach allows us to systematically investigate the influence of various parameters on the hydro- and sediment dynamics, since it enables the decomposition of all variables in the different tidal constituents, thus providing insight in the underlying physical mechanisms. The simplified model geometry has been based on bathymetric and hypsometric data of the Scheldt estuary and the model results for water levels, velocities, SSC and tidally averaged sand transport have been validated with recent field measurements to the extent possible.

The total tidally averaged sand transport is directed seaward close to the open boundary and then decreases along the estuary to eventually switch to a smaller landward transport, with a local peak in the vicinity of the landward boundary. There has been an increase over the years in the net sand export at the open boundary as well as in the landward sand transport close to the landward boundary. The behaviour of the total tidally averaged sand transport follows from a subtle balance between its different contributions. The advective contributions that result from the internally generated overtides result in landward sand transport, while the other contributions favour seaward sand transport. Historical changes in bathymetry and tidal forcing have influenced the various contributions to the total tidally averaged sand transport in different ways. More specifically, the model describes a competition between (the morphodynamic response to) bathymetric changes, which mainly influence the landward directed contributions, and the changes in tidal forcing, which strongly affect the seaward directed contributions. Close to the seaward boundary, the effect of the tidal forcing is dominant, such that an increase in tidal amplitude turns the balance between the contributions in favour of more seaward transport. More landward, both effects are more or less balanced, but close to the landward boundary, the bathymetric changes become the dominant effect, such that a deepening of the estuary leads to a stronger landward transport.

Furthermore, several sensitivity studies have been performed, regarding the response of the tidally averaged sand transport to future SLR. An increase of the mean sea-level leads to a change in the amplitudes of the different tidal constituents at the open boundary, as well as a change in their phases, due to a shift of the amphidromic points in the North Sea. Since the total tidally averaged sand transport is quite sensitive to changes in the tidal forcing and there is still quite some uncertainty in the predictions of the response of the tidal signal to SLR, it remains difficult to perform accurate long-term simulations of the sediment transport and the morphodynamics in estuaries, such as the Scheldt. Therefore, exploratory models, as the one presented in this paper, can be a valuable complementary tool to more complex simulation models in the search for better predictions

considering the effect of global warming. The model has shown that there is a competition between the effects of a higher mean sea-level and the associated changes in the different tidal constituents, which, in turn, compete with one another as well.

Appendix

A Tidal asymmetry

The tidal asymmetry affects the sediment transport by means of the advective terms. So, if we consider only the advective contributions to the sediment transport, we get

$$q_u \sim \langle uC \rangle \tag{A.1}$$

Looking at the dimensionless equation for the sediment concentration Eq. 2.10 and considering an approximate balance between erosion and deposition, assuming $\beta \sim 1$, we find that

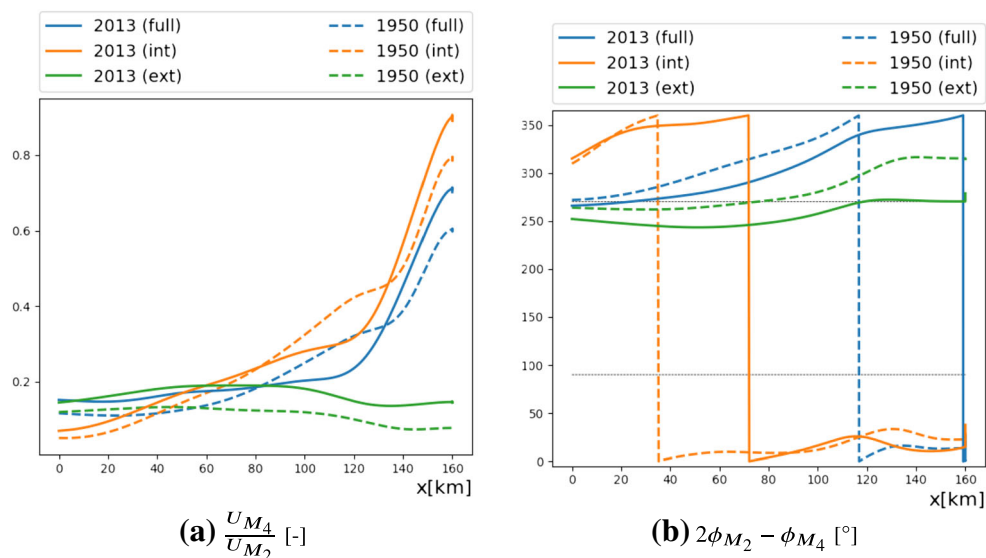$$C \approx |\mathbf{u}|^2. \tag{A.2}$$

In this case, the four contributions to the sediment transport $q_{u,\text{adv}}^{M_2,\text{int}}$, $q_{u,\text{adv}}^{M_4,\text{int}}$, $q_{u,\text{adv}}^{M_2,\text{ext}}$ and $q_{u,\text{adv}}^{M_4,\text{ext}}$ are simplified to the following two terms, as was explained in Boelens et al. (2018),

$$q_{u,\text{adv}}^{\text{int}} \sim U_{M_2}^2 U_{M_4}^{\text{int}} \cos(2\phi_{M_2} - \phi_{M_4}^{\text{int}})$$
$$= U_{M_2}^3 \frac{U_{M_4}^{\text{int}}}{U_{M_2}} \cos(2\phi_{M_2} - \phi_{M_4}^{\text{int}}) \tag{A.3}$$

$$q_{u,\text{adv}}^{\text{ext}} \sim U_{M_2}^2 U_{M_4}^{\text{ext}} \cos(2\phi_{M_2} - \phi_{M_4}^{\text{ext}})$$
$$= U_{M_2}^3 \frac{U_{M_4}^{\text{ext}}}{U_{M_2}} \cos(2\phi_{M_2} - \phi_{M_4}^{\text{ext}}). \tag{A.4}$$

These simplifications illustrate that only taking amplitude asymmetry into account would imply that the system is flood dominant, according to the definition of Friedrichs and Aubrey (1988) (as can be seen in Fig. 12a and b), and sediment would be transported in the landward direction throughout the channel. However, our model, which also includes other effects, such as temporal and spatial settling lag (de Swart and Zimmerman 2009), shows sediment transport in the seaward direction in the seaward part of the channel. Therefore, other transport mechanisms, included in Eq. 2.10, are essential to consider. This also shows that the widely used proxy from Friedrichs and Aubrey (1988), who

Fig. 12 Amplitude ratio and phase difference of the M_2 and M_4 tidal constituent of the longitudinal velocity. The parameters are shown for the internally generated (int, orange line) and the externally prescribed (ext, green line) M_4 component, as well as for the combined (full, blue lines) M_4 component

(a) $\frac{U_{M_4}}{U_{M_2}}$ [-]   **(b)** $2\phi_{M_2} - \phi_{M_4}$ [°]

only consider short channels ($L < 15\,\mathrm{km}$), is not valid for long systems, such as the Scheldt estuary.

References

Alnæs MS, Blechta J, Hake J, Johansson A, Kehlet B, Logg A, Richardson C, Ring J, Rognes ME, Wells GN (2015) The FEniCS project version 1.5. Archi Numer Softw 3(100):9–23. https://doi.org/10.11588/ans.2015.100.20553

Apecechea MI, Verlaan M, Zijl F, Le Coz C, Kernkamp H (2017) Effects of self-attraction and loading at a regional scale: a test case for the Northwest European Shelf. Ocean Dyn 67(6):729–749

Barneveld H, Nicolai R, van Veen M, van Haaster S, Boudewijn T, de Jong J, van Didderen K, van de Haterd R, Middenveld P, Michielsen S, Van De Moortel I, Velez C, de Wilde E (2018) Analyserapport: T2015-rapportage Schelde-estuarium. Tech. Rep. PR3152.10, HKV, Bureau Waardenburg and Antea. https://www.vnsc.eu/publicaties/wetenschappelijke-publicaties-en-rapporten/1070-t2015-rapportage-schelde-estuarium-analyserapport.html, in Dutch

Beullens J, Vandenbruwaene W, Meire D, Verwaest T, Mostaert F (2017) Historische evolutie getij en morfologie schelde estuarium: Analyse morfologie en getij - data analyse. Tech. Rep. WL2016R14_147_2 Flanders Hydraulics Research, Antwerp, Belgium, in Dutch

Bi Q, Toorman EA (2015) Mixed-sediment transport modelling in scheldt estuary with a physics-based bottom friction law. Ocean Dyn 65(4):555–587

Boelens T, Schuttelaars H, Schramkowski G, De Mulder T (2018) The effect of geometry and tidal forcing on hydrodynamics and net sediment transport in semi-enclosed tidal basins. Ocean Dyn 68(10):1285–1309

Bolle A, Wang ZB, Amos C, De Ronde J (2010) The influence of changes in tidal asymmetry on residual sediment transport in the Western Scheldt. Cont Shelf Res 30(8):871–882

Brouwer R, Schramkowski G, Mostaert F (2017) Geïdealiseerde processtudie van systeemovergangen naar hypertroebelheid: WP 1.3 Basismodel getij en zout. Tech. Rep. WL2017R13_103_3 Flanders Hydraulics Research, Antwerp, Belgium, in Dutch

Brouwer RL, Schramkowski GP, Dijkstra YM, Schuttelaars HM (2018) Time evolution of estuarine turbidity maxima in well-mixed, tidally dominated estuaries: the role of availability-and erosion-limited conditions. J Phys Oceanogr 48(8):1629–1650

Burchard H, Schuttelaars HM, Ralston DK (2018) Sediment trapping in estuaries. Ann Rev Mar Sci 10(1):371–395

Chen MS, Wartel S, Van Eck B, Van Maldegem D (2005) Suspended matter in the scheldt estuary. Hydrobiologia 540(1-3):79–104

Chernetsky AS, Schuttelaars HM, Talke SA (2010) The effect of tidal asymmetry and temporal settling lag on sediment trapping in tidal estuaries. Ocean Dyn 60(5):1219–1241

Chu A, Wang Z, De Vriend H (2015) Analysis on residual coarse sediment transport in estuaries. Estuar Coast Shelf Sci 163:194–205

Cleveringa J (2013) Grootschalige sedimentbalans van de wester-schelde. Project LTV Veiligheid en Toegankelijkheid LTV V&T-Rapport K-17, Arcadis (Emmeloord)

Coen L, De Maerschalck B, Plancke Y, Verwaest T, Mostaert F (2015) Sedimentstrategie beneden zeeschelde. deelrapport 1–opzet, validatie en scenarioberekeningen fase 1 met behulp van een numeriek sedimenttransportmodel. Tech. Rep. WL2015R14_025_1 Flanders Hydraulics Research, Antwerp, Belgium

de Swart H, Zimmerman J (2009) Morphodynamics of tidal inlet systems. Annual Rev Fluid Mech 41:203–229

Dijkstra YM, Brouwer RL, Schuttelaars HM, Schramkowski GP (2017) The iflow modelling framework v2. 4: a modular idealized process-based model for flow and transport in estuaries. Geosci Model Dev 10(7):2691–2713

Donatelli C, Ganju NK, Zhang X, Fagherazzi S, Leonardi N (2018) Salt marsh loss affects tides and the sediment budget in shallow bays. J Gophys Res Earth Surface 123(10):2647–2662

Dronkers J (1986) Tide-induced residual transport of fine sediment. Phys Shallow Estuaries Bays 16:228–244

Fagherazzi S, Kirwan ML, Mudd SM, Guntenspergen GR, Temmerman S, D'Alpaos A, van de Koppel J, Rybczyk JM, Reyes E, Craft C et al (2012) Numerical models of salt marsh evolution: ecological, geomorphic, and climatic factors. Reviews of Geophysics 50(1)

Friedrichs C, Armbrust B, De Swart H (1998) Hydrodynamics and equilibrium sediment dynamics of shallow, funnel-shaped tidal estuaries. Physics of estuaries and coastal seas: 315–327

Friedrichs CT, Aubrey DG (1988) Non-linear tidal distortion in shallow well-mixed estuaries: a synthesis. Estuar Coast Shelf Sci 27(5):521–545

Geuzaine C, Remacle JF (2009) Gmsh: A 3-D finite element mesh generator with built-in pre-and post-processing facilities. Int J Numer Methods Eng 79(11):1309–1331

Gräwe U, Burchard H, Müller M, Schuttelaars HM (2014) Seasonal variability in m2 and m4 tidal constituents and its implications for the coastal residual sediment transport. Geophys Res Lett 41(15):5563–5570

Hertoghs R, Vereecken H, Boeckx L, Deschamps M, Mostaert F (2018) Vijfjarig overzicht van de tijwaarnemingen in het zeescheldebekken: Tijdvak 2011-2015. Tech. Rep. WL2018R16_035_1 Flanders Hydraulics Research, Antwerp, Belgium, in Dutch

Hoffmann M, Meire P (1997) De oevers langs de zeeschelde: inventarisatie van de huidige oeverstructuren. WATER-BRUSSELS-pp 131–137

Idier D, Paris F, Le Cozannet G, Boulahya F, Dumas F (2017) Sea-level rise impacts on the tides of the european shelf. Cont Shelf Res 137:56–71

IPCC (2013) Climate change 2013: the physical science basis. Contribution of working group I to the fifth assessment report of the intergovernmental panel on climate change. Cambridge University Press, Cambridge. https://doi.org/10.1017/CBO9781107415324. www.climatechange2013.org

Kirwan ML, Megonigal JP (2013) Tidal wetland stability in the face of human impacts and sea-level rise. Nature 504(7478):53

Kirwan ML, Temmerman S, Skeehan EE, Guntenspergen GR, Fagherazzi S (2016) Overestimation of marsh vulnerability to sea level rise. Nat Clim Change 6(3):253

Kuijper K, Lescinski J (2013) Data analyses water levels ebb and flood volumes and bathymetries Western Scheldt. Tech. rep., International Marine & Dredging Consultants Deltares, Svašek Hydraulics BV, ARCADIS Nederland BV

Kumar M, Schuttelaars HM, Roos PC, Möller M (2016) Three-dimensional semi-idealized model for tidal motion in tidal estuaries. Ocean Dyn 66(1):99–118

Li C, O'Donnell J (2005) The effect of channel length on the residual circulation in tidally dominated channels. J Phys Oceanogr 35(10):1826–1840

Li C, Valle-Levinson A (1999) A two-dimensional analytic tidal model for a narrow estuary of arbitrary lateral depth variation: The intratidal motion. J Geophys Res Oceans 104(C10):23,525–23,543

Lorentz H (1922) Het in rekening brengen van den weerstand bij schommelende vloeistofbewegingen. De ingenieur

Maris T, Meire P (2016) Omes rapport 2015. Onderzoek naar de gevolgen van het Sigmaplan, baggeractiviteiten en havenuitbreiding in de Zeeschelde op het milieu Universiteit Antwerpen: Antwerpen

Meire P, Van Dyck M (2014) Naar een duurzaam rivierbeheer: hoe herstellen we de ecosysteemdiensten van rivieren? De Schelde als blauwe draad. University Press Antwerp

Müller M, Cherniawsky JY, Foreman MG, von Storch JS (2014) Seasonal variation of the M_2 tide. Ocean Dyn 64(2):159–177

Murray AB (2003) Contrasting the goals, strategies, and predictions associated with simplified numerical models and detailed simulations. Prediction in geomorphology, pp 151–165

Nnafie A, Van Oyen T, De Maerschalck B, Plancke Y, Verwaest T, Mostaert F (2016) Modeling effects of geometry, initial bathymetry and sediment availability on the morphodynamic evolution of the scheldt mouth area. Tech. Rep. WL2016R14_094 Flanders Hydraulics Research, Antwerp, Belgium

Nnafie A, Van Oyen T, De Maerschalck B, van der Vegt M, Wegen MVD (2018) Estuarine channel evolution in response to closure of secondary basins: an observational and morphodynamic modeling

study of the western scheldt estuary. J Gophys Res Earth Surface 123(1):167–186

Pickering M, Horsburgh K, Blundell J, Hirschi JM, Nicholls RJ, Verlaan M, Wells N (2017) The impact of future sea-level rise on the global tides. Cont Shelf Res 142:50–68

Pickering M, Wells N, Horsburgh K, Green J (2012) The impact of future sea-level rise on the european shelf tides. Cont Shelf Res 35:1–15

Ridderinkhof W, de Swart H, van der Vegt M, Alebregtse N, Hoekstra P (2014) Geometry of tidal inlet systems: a key factor for the net sediment transport in tidal inlets. J Geophys Res Oceans 119(10):6988–7006

Schuttelaars H, de Swart H (2000) Multiple morphodynamic equilibria in tidal embayments. J Geophys Res Oceans (1978–2012) 105(C10):24,105–24,118

Taverniers E, Plancke Y, Mostaert F (2013) Moneos-jaarboek monitoring wl-basisboek: Overzicht monitoring hydrodynamiek en fysische parameters zoals door wl in het zeescheldebekken gemeten-uitleggend basisboek met algemene situering, methodologie en achtergrond. WL Rapporten

Temmerman S, Govers G, Wartel S, Meire P (2004) Modelling estuarine variations in tidal marsh sedimentation: response to changing sea level and suspended sediment concentrations. Mar Geol 212(1-4):1–19

Ter Brake MC, Schuttelaars HM (2010) Modeling equilibrium bed profiles of short tidal embayments. Ocean Dyn 60(2):183–204

Ter Brake MC, Schuttelaars HM (2011) Channel and shoal development in a short tidal embayment: an idealized model study. J Fluid Mech 677:503–529

Townend I, Pethick J (2002) Estuarine flooding and managed retreat. Philosophical Transactions of the Royal Society of London Series A: Mathematical. Phys Eng Sci 360(1796):1477–1495

Van Braeckel A, Piesschaert F, Van den Bergh E (2007) Historische analyse van de Zeeschelde en haar getijdegebonden zijrivieren: 19e eeuw tot heden. INBO

van der Spek AJF (1994) Large-scale evolution of Holocene tidal basins in the Netherlands. Faculteit Aardwetenschappen, phD-thesis, Universiteit Utrecht

Van der Werf J, Briere C (2013) The influence of morphology on tidal dynamics and sand transport in the Scheldt estuary. Tech. rep., The Netherlands: Consortium Deltares IMDC, Svašek, Arcadis

van Maren DS, Winterwerp JC, Vroom J (2015) Fine sediment transport into the hyper-turbid lower ems river: the role of channel deepening and sediment-induced drag reduction. Ocean Dyn 65(4):589–605

Van Rijn L (2013) Tidal phenomena in the scheldt estuary, part 2. Tech. rep., International Marine & Dredging Consultants Deltares, Svašek Hydraulics BV, ARCADIS Nederland BV

Verlaan M, De Kleermaeker S, Buckman L et al (2015) Glossis: Global storm surge forecasting and information system. In: Australasian Coasts & Ports Conference 2015: 22nd Australasian Coastal and Ocean Engineering Conference and the 15th Australasian Port and Harbour Conference, Engineers Australia and IPENZ, p 229

Verlaan PAJ (1998) Mixing of marine and fluvial particles in the scheldt estuary. PhD thesis, TU Delft

Vroon J, Storm C, Coosen J (1997) Westerschelde, stram of struis? eindrapport van het project oostwest, een studie naar de beïnvloeding van fysische en verwante biologische patronen in een estuarium. Tech. Rep. Rapport RIKZ-97.023 Rijkswaterstaat, Rijksinstituut Kust en Zee, Middelburg, in Dutch

Wahl T, Haigh ID, Woodworth PL, Albrecht F, Dillingh D, Jensen J, Nicholls RJ, Weisse R, Wöppelmann G (2013) Observed mean sea level changes around the north sea coastline from 1800 to present. Earth Sci Rev 124:51–67

Wang Z, Hoekstra P, Burchard H, Ridderinkhof H, De Swart H, Stive M (2012) Morphodynamics of the Wadden Sea and its barrier island system. Ocean & Coastal Management 68:39–57

Wang Z, Jeuken M, Gerritsen H, De Vriend H, Kornman B (2002) Morphology and asymmetry of the vertical tide in the Westerschelde estuary. Cont Shelf Res 22(17):2599–2609

Ward SL, Green JM, Pelling HE (2012) Tides, sea-level rise and tidal power extraction on the european shelf. Ocean Dyn 62(8):1153–1167

Wei X, Kumar M, Schuttelaars HM (2018) Three-dimensional sediment dynamics in well-mixed estuaries: importance of the internally generated overtide, spatial settling lag, and gravitational circulation. J Geophys Res Oceans 123(2):1062–1090

Zimmerman J (1982) On the Lorentz linearization of a quadratically damped forced oscillator. Phys Lett A 89(3):123–124